Simulation of hydrogen embrittlement of steel using mixed nonlocal finite elements

Daniella Lopes Pinto, Amar El Ouazani Tuhami, Nikolay Osipov, Yazid Madi, Jacques Besson

Highlights

Simulation of hydrogen embrittlement of steel using mixed nonlocal finite elements

Daniella Lopes Pinto,Amar El Ouazani Tuhami,Nikolay Osipov,Yazid Madi,Jacques Besson

- A new multi-field simulation strategy to model hydrogen embrittlement is proposed.
- Application of the strategy to an existing experimental database.
- Simulation of tensile, fracture toughness, and pressurized disk tests.
- The model represents the effect of loading rate on ductility.
- The model illustrates the decrease in toughness caused by hydrogen.

Simulation of hydrogen embrittlement of steel using mixed nonlocal finite elements

Daniella Lopes Pinto[a,b], Amar El Ouazani Tuhami[b], Nikolay Osipov[b], Yazid Madi[a] and Jacques Besson[a,*]

[a]*Mines Paris, PSL Research University, Centre des Matériaux,CNRS UMR 7633, 63–65 rue Henri-Auguste Desbruères, Corbeil-Essonnes, 91003, France*
[b]*Transvalor S.A., 950 Avenue Roumanille CS 40237, Biot, 06904, Sophia Antipolis Cedex, France*

ARTICLE INFO

Keywords:
Hydrogen embrittlement
Mixed formulation
Nonlocal damage
GTN model

ABSTRACT

A new simulation strategy to model hydrogen embrittlement based on a multi-field finite element using displacements, pressure, volume variation, nonlocal damage variables and lattice hydrogen concentration as unknowns is proposed. The material is described using a modified GTN model, which includes the description of hydrogen enhanced decohesion (HEDE). The finite element problem is solved using a fully implicit formulation. Numerical problems related to volumetric locking are solved using a mixed pressure/volume variation formulation. The use of the mixed formulation allows a straightforward evaluation of the pressure gradient, which drives hydrogen diffusion. Mesh size dependence is solved using an implicit gradient nonlocal formulation. Two variables are used to represent damage: the plastic volume variation and the accumulated plastic strain, controlling nucleation. The model is used to simulate an existing experimental database (Moro et al., 2010; Briottet et al., 2012) including tensile, fracture toughness and pressurized disk tests. The model, after adjusting the various coefficients, can represent the main experimental findings: the effect of deformation rate on the failure of tensile specimens, the transition from surface to internal fracture with increasing deformation rate, the sharp toughness drop under hydrogen (CT specimen), the fracture location and the effect of the pressurization rate in the case of the tests on disks.

1. Introduction

As the power demand continuously grows and the need to address global warming becomes more urgent, there is a pressing need for new energy sources that can effectively contribute to decarbonization efforts. Hydrogen, produced from water using renewable energy sources or nuclear energy, is emerging as a promising solution as a clean and renewable energy vector (Abbasi, 2011; Meibom and Karlsson, 2010). It has the potential to help decarbonize the energy sector and achieve climate goals.

However, a critical challenge when using hydrogen as an energy vector is its ability to readily diffuse through metals and accumulate at high-stress locations, leading to premature failure characterized by reduced ductility and toughness. This phenomenon, known as hydrogen

ORCID(s): 0000-0003-1975-2408 (J. Besson)

embrittlement (HE) (Hirth, 1980; Sofronis and McMeeking, 1989; Robertson et al., 2015), is a complex phenomenon that involves a combination of mechanical and chemical factors. Therefore, understanding the hydrogen embrittlement phenomenon and the long-term behavior of metals in industrial power generation and transmission structures is essential to ensure their safety and reliability.

The hydrogen embrittlement phenomenon has been widely studied, and several mechanisms have been proposed to explain it, including Hydrogen Enhanced Localized Plasticity (HELP) (Ferreira et al., 1999; Beachem, 1972; Barnoush and Vehoff, 2010), Hydrogen Enhanced Decohesion (HEDE) (Troiano, 2016; Gerberich et al., 1994), and Hydrogen Enhanced Strain-Induced Vacancy (HESIV) (Nagumo et al., 2001). The HELP mechanism proposes that hydrogen increases dislocation mobility near crack tips, which locally enhances plasticity. This mechanism leads to reduced fracture toughness and increased susceptibility to brittle fracture. On the other hand, according to the HEDE mechanism, hydrogen weakens the cohesive strength of the atomic bonds in the material lattice, leading to the separation of atoms. The HESIV mechanism occurs when hydrogen atoms enhance the formation of vacancies in the metal lattice, which is believed to weaken the metal and make it more prone to fracture (Depraetere et al., 2021; Nagumo, 2004). It should be noted that all of these mechanisms can operate concurrently or independently, leading to a degradation of the mechanical properties of metals subjected to hydrogen embrittlement. Further research is needed to fully understand the interaction between these mechanisms and to develop effective strategies for preventing hydrogen embrittlement.

In order to accurately model hydrogen embrittlement, it is essential to consider its degrading impact on the mechanical properties of materials. Specifically, a damage mechanism that is influenced by the hydrogen concentration must be implemented to simulate the accelerated evolution of damage. The cohesive zone modeling (CZM) is a popular approach employed in several studies on hydrogen embrittlement simulations at the continuum level (Ahn et al., 2007; Xia et al., 2019; Olden et al., 2008; Jemblie et al., 2017; Xia et al., 2019). In this model, cohesive elements are introduced along a predefined crack path. The effect of hydrogen embrittlement is then incorporated by reducing the cohesive strength with increasing hydrogen concentration. Alternatively, the phase-field approach has also been utilized as an alternative to CZM in recent research (Martínez-Pañeda et al., 2018). In this approach, the material is represented as a continuous field where each point in space corresponds to the local composition and state of the material, and the evolution of this field over time is governed by a set of partial differential equations that describe the diffusion of hydrogen and the mechanical response of the material. Notably, both the phase-field and cohesive zone model approaches can be used to describe the HEDE mechanism. The Gurson-Tvergaard-Needleman (GTN) model, a widely used micromechanical model that describes the ductile rupture of materials, was also modified to account for hydrogen embrittlement (Yu et al., 2019; Lin et al., 2022b; Depraetere et al., 2021). It can also be used together with a CZM approach as in (Lin et al., 2022a). In that case, the GTN model describes ductile fracture, whereas the CZM describes quasi-brittle fracture induced by hydrogen.

In this study, a strategy is proposed to simulate hydrogen embrittlement using the finite element method. The material behavior is described using the GTN model, which is modified to account for the effect of hydrogen. The simulation approach, therefore, integrates plasticity and damage and takes into consideration the coupling with hydrogen diffusion. To mitigate volumetric locking, a mixed formulation in displacement, pressure, and volume variation (Zhang et al., 2018;

Bellet, 1999; Taylor, 2000) is employed. It allows a better evaluation of the hydrostatic pressure, which plays a key role in both damage growth and hydrogen diffusion. To address the mesh dependence problem associated with the use of models describing damage, an implicit gradient nonlocal formulation with two internal lengths is employed (Peerlings et al., 1996; Seupel et al., 2020; El Ouazani Tuhami et al., 2022). This allows the regularization of void growth and strain-controlled nucleation, contributing to a more reliable representation of the hydrogen embrittlement phenomenon.

The paper is organized as follows: Section 2 presents the formulation of the nonlocal Gurson-Tvergaard-Needleman model. In section 3, the hydrogen transport equations are presented, along with the coupling of the GTN model with these equations and an overview of different hypotheses present in the literature. Section 4 provides details on the finite element implementation of the proposed formulation and considers the boundary conditions for the diffusion problem. Finally, sections 5 and 6 present the simulations that are conducted to test the proposed model and compare the results with an existing database. The obtained results are discussed, with a focus on the influence of loading methods and applied boundary conditions.

2. Nonlocal GTN model

The GTN, like other continuum models including damage, introduces softening of the material up to failure. This causes pathological mesh dependence when the model is implemented in a standard displacement-based FE formulation. This is caused by the formation of localized strain and damage bands having an undetermined width (Rice, 1976; Rudnicki and Rice, 1975; Tvergaard, 1982). To solve this problem, the so-called nonlocal models can be used. They introduce material internal lengths, which are missing in standard damage models. Several solutions have been proposed in the literature and are briefly reviewed in the following, focusing on the application to ductile rupture.

The first solution is based on a local enrichment by embedding a finite thickness band (Huespe et al., 2009) proposed to enrich the kinematics within elements by embedding a finite thickness band. The band is introduced when localization is detected, following Rice (1976) bifurcation analysis, which also provides the orientation of the newly introduced band. The implicit gradient model (Mediavilla et al., 2006; Linse et al., 2012; Hütter et al., 2013; Javani et al., 2016; Seupel et al., 2020; Leclerc et al., 2020) is a relatively easy way to introduce material lengths. It can be interpreted (Peerlings et al., 1996) as an approximation of integral methods originally proposed in (Pijaudier-Cabot and Bazant, 1987; Bazant and Pijaudier-Cabot, 1988) for quasi-brittle materials, but which can also be applied to ductile fracture (Tvergaard and Needleman, 1995; Enakoutsa et al., 2007). Another approach is based on micromorphic models (Forest, 2009), which can be used to model ductile failure as in (Brepols et al., 2017; Diamantopoulou et al., 2017). A nonlocal gradient enhanced energy (GEE) model has also been proposed in the case of ductile failure (Zhang et al., 2018; Chen et al., 2020). The model uses the accumulated plastic strain, which is defined locally (at Gauss point) and globally. To weakly enforce the equality between both variables, which represent the same physical quantity, Lagrange multipliers are introduced. The free energy is expressed so as to penalize strong gradients thus leading to regularization. It is shown in (Scherer et al., 2020) that this model can be interpreted as a limit case of the micromorphic model, in which the micromorphic variable and its counterpart are forced to be equal. Finally, phase-field models can also be used. They were initially introduced to describe brittle failure (Tanné et al., 2018), but have also been employed in the case of ductile failure, as in (Ambati et al., 2015; Eldahshan et al., 2021; Miehe et al., 2016). Recently, the GTN model was applied within this framework (Dittmann et al., 2020). Furthermore, this same framework has been utilized for modeling hydrogen embrittlement in metals, as preivously mentioned (Martínez-Pañeda et al., 2018).

In this work, the implicit gradient model integrating two material lengths proposed by El Ouazani Tuhami et al. (2022) is used. The model introduces two nonlocal variables: $\overline{\omega}$, corresponding to the plastic volume change and $\overline{\kappa}$, corresponding to the accumulated plastic strain. $\overline{\kappa}$ is used to describe damage nucleation and does not affect hardening as in (Peerlings et al., 2012). Based on the formulation of the GTN model proposed in (Besson et al., 2001), an effective scalar stress $\sigma_\star$ can be implicitly defined by:

$$\Phi = \frac{\sigma_{\text{eq}}^2}{\sigma_\star^2} + 2q_1 f_\star \cosh\left(\frac{q_2}{2}\frac{\sigma_{kk}}{\sigma_\star}\right) - 1 - q_1^2 f_\star^2 \quad \overset{\text{def. } \sigma_\star}{=} \quad 0 \tag{1}$$

where σ_{eq} is the von Mises stress, σ_{kk} the trace of the stress tensor ($\boldsymbol{\sigma}$). $f_\star$ is a function of damage and q_1 and q_2 are model parameters. The yield surface is then given by:

$$\phi = \sigma_\star - \sigma_F(\kappa) \tag{2}$$

where σ_F is the flow stress, expressed as a function of the accumulated plastic strain κ. Plastic flow is obtained assuming normality and the plastic strain rate tensor is expressed as:

$$\dot{\boldsymbol{\varepsilon}}_p = (1 - f_g)\dot{\kappa}\frac{\partial \phi}{\partial \boldsymbol{\sigma}} = (1 - f_g)\dot{\kappa}\frac{\partial \sigma_\star}{\partial \boldsymbol{\sigma}} \tag{3}$$

where f_g represents the porosity due to void growth. Noting that $\sigma_\star$ is an homogenous function of degree 1 of $\boldsymbol{\sigma}$, one gets (Euler's Lemma) that:

$$\dot{\boldsymbol{\varepsilon}}_p : \boldsymbol{\sigma} = (1 - f_g)\dot{\kappa}\sigma_\star \tag{4}$$

In this work, the material is assumed to be slightly rate dependent, so that $\dot{\kappa}$ is expressed as:

$$\dot{\kappa} = \dot{\kappa}_0 \left\langle \frac{\sigma_\star - \sigma_F}{\sigma_0} \right\rangle^n \tag{5}$$

where $\dot{\kappa}_0$, σ_0 and n are material parameters. An additive strain decomposition is used so that the strain tensor is expressed as $\boldsymbol{\varepsilon} = \boldsymbol{\varepsilon}_e + \boldsymbol{\varepsilon}_p$, where $\boldsymbol{\varepsilon}_e$ is the elastic strain tensor. The stress tensor is given by $\boldsymbol{\sigma} = \mathbb{E} : \boldsymbol{\varepsilon}_e$, where $\mathbb{E}$ is the fourth order elasticity tensor. A finite deformation consistent with the additive strain decomposition is used in the following (section 4.3).

Nonlocal effects are introduced in the description of damage. The evolution of the porosity is expressed as:

$$\dot{f}_g = (1 - f_g)\dot{\overline{\omega}} \tag{6}$$

where $\overline{\omega}$ is the nonlocal counterpart of the volume change $\omega = \text{trace}\left(\dot{\boldsymbol{\varepsilon}}_p\right)$. The material is also affected by the nucleation of damage, which is assumed to be strain-controlled. The damage nucleation rated is expressed as:

$$\dot{f}_n = A(\overline{\kappa}, \dots)\dot{\overline{\kappa}} \tag{7}$$

where A is the damage nucleation rate. A is very often expressed following Chu and Needleman (1980), who assumed that the nucleation strain is distributed in a normal fashion. Other expressions can indeed be used as in (Zhang et al., 2000; Tanguy et al., 2008). The total damage inside of the material is given by: $f_t = f_g + f_n$. It is also possible to use a nucleation rate depending on stress triaxiality (Dalloz et al., 2009) or on the maximum principal stress (Petit et al., 2019). The $f_\star$ damage function is expressed following the original GTN model:

$$f_\star = \begin{cases} f_g + f_n & \text{if } f_g + f_n < f_c \\ f_c + \dfrac{f_g + f_n - f_c}{f_R - f_c}\left(\dfrac{1}{q_1} - f_c\right) & \text{otherwise} \end{cases} \tag{8}$$

where f_c represents damage at the onset of coalescence, f_c is the porosity at the onset of coalescence and f_R the porosity at failure. Failure occurs when $f_\star = 1/q_1$. In practice, the material points are considered as "broken" when $f_\star = 0.99/q_1$. As outlined in (El Ouazani Tuhami et al., 2022), eq. 6 slightly differ from the original formulation, where $\dot{f}_g$ would be expressed as $\dot{f}_g = (1 - f_g - f_n)\overline{\omega}$. The reason is that nucleation on primary inclusions, such as MnS, TiN and oxides in steel occurs at the early stages of deformation, so their volume fraction is usually considered as the initial values of the porosity f_0. Nucleation on iron carbides (Fe_3C) and quasi-cleavage resulting from hydrogen embrittlement lead to minimal extra-porosity, either due to the small size of carbides or the formation of micro-cracks.

Finally, the evolution of $\overline{\omega}$ and $\overline{\kappa}$ is governed by the following Helmholtz-type equations:

$$\overline{\omega} - l_\omega^2 \Delta\overline{\omega} = \omega \tag{9}$$

$$\overline{\kappa} - l_\kappa^2 \Delta\overline{\kappa} = \kappa \tag{10}$$

where l_ω and l_κ are two characteristic lengths that may differ. The following natural boundary conditions are used:

$$\boldsymbol{\nabla}\overline{\omega}.\boldsymbol{n} = 0 \qquad \boldsymbol{\nabla}\overline{\kappa}.\boldsymbol{n} = 0 \tag{11}$$

where $\boldsymbol{n}$ is the normal vector to the surface of the considered body.

It is important to note that the use of the implicit gradient model to describe both damage and strain gradient plasticity may lead to inconsistencies, as pointed out in (Forest, 2009; Peerlings et al., 2012). In the present framework, this would lead to expressing σ_F as a function of $\overline{\kappa}$ instead of κ in eq. 2. If strain gradient plasticity effects are to be considered as in (Martínez-Pañeda et al., 2016), micromorphic models (Forest, 2009) or gradient enhanced models (Chen et al., 2020) could be used to simultaneously deal with damage. They, however, offer less flexibility if several nonlocal variables are used. Using the present model, possible hardening due to plasticity gradients close to notches or cracks is not represented.

3. Model for hydrogen diffusion and coupling with the GTN model

3.1. Hydrogen transport

The prevailing theory for hydrogen transport in steels was proposed by Sofronis and McMeeking (1989) and later corrected by Krom et al. (1999). It is assumed that hydrogen atoms are either located in the lattice (concentration: C_L) or in the trapping sites (concentration: C_T). Only lattice atoms can diffuse and the total concentration is given by: $C = C_L + C_T$. The hydrogen flux is expressed as:

$$\boldsymbol{J} = -D_L \boldsymbol{\nabla} C_L + \frac{D_L C_L V_H}{RT} \boldsymbol{\nabla} p. \tag{12}$$

where p is the pressure ($\sigma_{kk}/3$), D_L the diffusion coefficient, R the gas constant, T the temperature and V_H the partial molar volume of hydrogen. The pressure gradient term is such that hydrogen will preferably diffuse toward highly stressed regions, such as notches or crack tips. The concentrations are expressed as functions of the occupancy of lattice (θ_L) and trapping sites (θ_T) as:

$$C_L = \beta N_L \theta_L \quad \text{and} \quad C_T = N_T \theta_T \tag{13}$$

where N_L is the number of lattice atoms per unit volume and N_T the trap density. β is the number of interstitial lattice sites per lattice atom, so that βN_L is the number of lattice sites per unit volume. $\beta = 6$ for BCC metals. θ_L and θ_T respectively represent the occupancy of lattice and trap sites. One generally assumes that $\theta_L \ll 1$. Lattice and trapped atoms are in instantaneous equilibrium following the model by Oriani (1970), so that:

$$\frac{\theta_T}{1-\theta_T} = \frac{\theta_L}{1-\theta_L} \exp(W_B/RT) \tag{14}$$

where W_B is the trap binding energy. It is also possible to account for the trapping/detrapping kinetics as in *e.g.* (Benannoune et al., 2019). Accounting for trapping/detrapping kinetics is also important in the case of hydrogen in zirconium alloys, where trapping and detrapping respectively correspond to hydride precipitation and dissolution (Xia et al., 2019). The trapping sites are assumed to be dislocations, so that the trapping density can be expressed as (Taha and Sofronis, 2001; Shibata et al., 2021): $N_T = \sqrt{2}\rho/a$, where a is the lattice parameter and ρ is the dislocation density, which is related to the accumulated plastic strain. It is also possible to directly express N_T as a function of the accumulated plastic strain κ (Sofronis and McMeeking, 1989; Depraetere et al., 2021; Briottet et al., 2012). More advanced and complex models can integrate multiple trapping sites (Benannoune et al., 2019).

Using eq. 13 together with eq. 14 and assuming $\theta_L \ll 1$, C_T can be expressed as:

$$C_T = N_T \frac{\Xi C_L}{1 + \Xi C_L} \quad \text{with } \Xi = \exp(W_B/RT) \frac{1}{N_L \beta} \tag{15}$$

taking the time derivative of C_T, one gets:

$$\dot{C}_T = \frac{1}{N_T} \frac{dN_T}{d\overline{\kappa}} C_T \dot{\overline{\kappa}} + \frac{\Xi N_T}{(1+\Xi C_L)^2} \dot{C}_L = h + H_{C_L} \dot{C}_L \tag{16}$$

3.2. Coupling with the GTN model

Considering the HELP embrittlement mechanism, the flow stress of the material should be a decreasing function of the hydrogen concentration, as for instance proposed by Ahn et al. (2007), where it is proposed to express the flow stress as:

$$\sigma_F(\kappa, C) = \sigma_F^0(\kappa) \times \xi(C) \tag{17}$$

where σ_F^0 is the flow stress in absence of hydrogen and ξ an *ad hoc* function. The yield surface (eq. 2) for the voided solid therefore remains unchanged and can be expressed now as: $\phi = \sigma_\star - \sigma_F(\kappa, C)$. Faleskog et al. (1998) demonstrated through unit cell simulations that the GTN model's q_1 and q_2 parameters rely on hardening, hence on C, with hydrogen influencing the hardening. Changes in q_1 and q_2 will directly affect the void growth kinetics. Moreover, diffusion of hydrogen at microscale around voids may further modify the growth kinetics and lead to earlier failure (Ahn et al., 2007; Yu et al., 2019). It was proposed by Depraetere et al. (2021) to modify the void growth kinetics as: $\dot{f}_g = \dot{f}_g^0(1 + k_g^L C_L + k_g^T C_T)$, where $\dot{f}_g^0$ is the kinetics in absence of hydrogen. It assumes that q_1 and q_2 remain constant and can be fitted using the hydrogen-free material. k_g^L and k_g^T are coefficients to be determined. This solution was also used by Lin et al. (2022b) without assuming different contributions of C_L and C_T leading to: $\dot{f}_g = \dot{f}_g^0(1 + k_g C)$, where k_g is again a coefficient to be fitted. Using these modified expressions, the initial void growth kinetics ($\dot{f}_g = (1 - f_g)\mathrm{trace}\dot{\boldsymbol{\varepsilon}}_p$) no longer holds. As this equation represents mass conservation, it appears to be desirable not to modify it. For that reason, it is proposed in that study to express q_1 and q_2 as functions of C (or possibly of C_L and C_T) to represent the acceleration of growth in presence of hydrogen.

Following Depraetere et al. (2021), the nucleation rate could also be modified. Following the same guidelines as for growth, it was proposed to express the nucleation rate in presence of hydrogen as: $\dot{f}_n = \dot{f}_n^0(1 + k_n^L C_L + k_n^T C_T)$ (or as $\dot{f}_n = \dot{f}_n^0(1 + k_n C)$ in (Lin et al., 2022b)), where $\dot{f}_n^0$ is the nucleation rate in absence of hydrogen. k_n^L and k_n^T (or k_n) are parameters which need to be adjusted. In steels, nucleation corresponds to the cracking or debonding of iron carbides as coarse inclusions (MnS, CaS, TiN…) are assumed to debond or crack at the onset of plasticity, and are therefore assumed to correspond to the initial porosity. Hydrogen may facilitate these processes, so that the solution proposed in (Depraetere et al., 2021) will also be used in this work. It is proposed to also describe HEDE as the nucleation of damage. As this mechanism is not present in the hydrogen-free material, a specific term must be added. Consequently, the following nucleation kinetics is proposed:

$$\dot{f}_n = A(\overline{\kappa}, \dots)\zeta(C, \dots)\dot{\overline{\kappa}} + B(\sigma_I, C, \dots)\dot{\overline{\kappa}} \tag{18}$$

where A represents nucleation on carbides and is assumed to be strain-controlled. ζ represents the acceleration of nucleation caused by hydrogen. Additionally, B stands for HEDE and is dependent, *a priori*, on the maximum principal stress (σ_I) to account for the quasi-brittle nature associated with this damage mechanism. A proposal for the B function is presented at section 5.1. In (Ahn et al., 2007; Lin et al., 2022a) a cohesive zone model was used for that purpose. The proposed solution avoids the need for predefining a crack path, which can be useful in the case of multiple cracks or crack bifurcation. The trap density N_T is expressed as a function of the nonlocal accumulated plastic strain $\overline{\kappa}$, which avoids strong localization of C_T and allows consistent control of damage nucleation.

In this section, a comprehensive framework was introduced, which facilitates the coupling of the GTN model with hydrogen embrittlement. This, indeed, does not mean that all possibilities should be used simultaneously. For instance, in the case where quasi-brittle failure is the main failure mechanism, the model can be simplified by setting $q_2 = 0$ (no void growth), neglecting ductile damage nucleation ($A = 0$) and only using an *ad hoc* B function to represent damage development. The coupling also allows describing the transition from pure ductile failure to pure quasi-brittle failure using a single model, which appears important to represent the effect of the loading rate on the failure mode.

4. Implementation

4.1. Finite element discretization

The proposed model was implemented in the Z-set software (Besson and Foerch, 1997) developed at Mines Paris and ONERA[1]. To better control pressure and avoid volumetric locking, mixed elements are used. The unknowns for the mechanical problem are therefore: nodal displacements ($\{\boldsymbol{u}\}$), nodal pressures ($\{p\}$) and nodal volume variations ($\{\theta\}$) (Bellet, 1999; Taylor, 2000; Zhang et al., 2018). The treatment of nonlocal variables ($\{\overline{\omega}\}$ and $\{\overline{\kappa}\}$) introduces two additional nodal fields of unknowns (El Ouazani Tuhami et al., 2022). Finally, diffusion of the lattice hydrogen introduces a sixth field ($\{C_L\}$). Positions and displacements are interpolated using quadratic shape functions, whereas the other fields are obtained using linear shape functions. Reduced integration is always used. Fig. 1 illustrates the element discretization in the case of square and triangle elements.

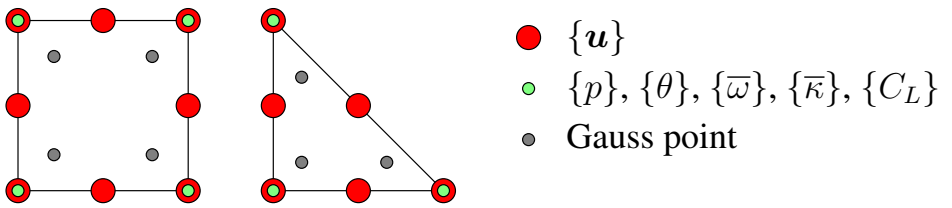

Figure 1: Square and triangular elements.

Using the mixed formulation, the pressure is defined at nodes, so that its gradient can be directly computed from nodal values. This avoids the procedure in which the hydrostatic stresses determined at Gauss points are extrapolated at nodes, so as to be able to compute the gradient. Such a procedure is described by Krom et al. (1999) in the appendix.

A monolithic time-integration scheme is used in this study. A staggered scheme solving *e.g.* for $(\boldsymbol{u}, p, \theta)$, then for $\overline{\omega}$, $\overline{\kappa}$ and finally C_L could also be used, as in (Mediavilla et al., 2006) in the case of an implicit gradient model. It is believed that the monolithic scheme, although more difficult to implement, provides a more stable and reliable solution.

4.2. Implementation of the constitutive equations

Following the generic representation of constitutive equations proposed by Foerch et al. (1997), their implementation in the FE code consists of a time-integration for given input variables ($\boldsymbol{V}_I$) to obtain output variables ($\boldsymbol{V}_0$). At the same time, variables representing the state of the material ($\boldsymbol{V}_{\text{in}}$) are also integrated. The integration is performed over a time increment $[t, t+\Delta t]$ and all variables are known at t. $\boldsymbol{V}_I$ are obtained at $t+\Delta t$ from elementary nodal values. In the case of the material model presented above, these "abstract" sets of data are:

$$\begin{aligned} \boldsymbol{V}_I &= (\boldsymbol{\varepsilon}, \overline{\omega}, \overline{\kappa}, C_L, \boldsymbol{\nabla} C_L, \boldsymbol{\nabla} p) \\ \boldsymbol{V}_0 &= (\boldsymbol{\sigma}, \omega, \kappa, \boldsymbol{J}, h, H_{C_L}) \\ \boldsymbol{V}_{\text{in}} &= (\boldsymbol{\varepsilon}_e, f_g, f_n, N_T, N_L, \theta_T, \theta_L) \end{aligned} \tag{19}$$

[1] `http://www.zset-software.com`

Where h and H_{C_L} are related to the variation in C_L caused by trapping/detrapping (see eq. 16). Note that the number of input/output variables may differ. In order to be able to compute the elementary stiffness matrices, the consistent tangent matrix must be evaluated. It is formally expressed as:

$$\boldsymbol{M} = \frac{\partial \boldsymbol{V}_0}{\partial \boldsymbol{V}_I} = \begin{pmatrix} \boldsymbol{M}_{\sigma\epsilon} & \boldsymbol{M}_{\sigma\overline{\omega}} & \cdots \\ \boldsymbol{M}_{\omega\epsilon} & \boldsymbol{M}_{\omega\overline{\omega}} & \cdots \\ \cdots & \cdots & \ddots \end{pmatrix} \tag{20}$$

The calculation of this matrix can be done piecewise with *e.g.*: $\boldsymbol{M}_{\sigma\epsilon} = \partial\boldsymbol{\sigma}/\partial\boldsymbol{\varepsilon}$. The constitutive equations are integrated using a fully implicit integration scheme following the methodology presented *e.g.* in (Scherer et al., 2020).

4.3. Mixed element formulation: finite strains and stresses

Following (Taylor, 2000), the virtual power principle for a mixed formulation can be expressed as:

$$\int_\Omega \left[\left(\mathbb{K} : \dot{\boldsymbol{\varepsilon}} + \frac{1}{3}\dot{\theta}\mathbf{1} \right) : \boldsymbol{\sigma}^\star + \dot{p}(\mathrm{trace}\boldsymbol{\varepsilon} - \theta) + (\mathrm{trace}\dot{\boldsymbol{\varepsilon}} - \dot{\theta})p \right] d\Omega + \dot{\Pi}_e = 0 \tag{21}$$

or after rearranging the previous equation:

$$\int_\Omega \left[\dot{\boldsymbol{\varepsilon}} : \boldsymbol{\sigma} + \dot{\theta} \left(\frac{1}{3}\mathrm{trace}\boldsymbol{\sigma}^\star - p \right) + \dot{p}(\mathrm{trace}\boldsymbol{\varepsilon} - \theta) \right] d\Omega + \dot{\Pi}_e = 0 \tag{22}$$

where $\mathbb{K}$ represents a fourth-order tensor that associates a second-order tensor to its deviator. The symmetric part of the velocity gradient is denoted as $\dot{\boldsymbol{\varepsilon}}$. The stress tensor $\sigma^\star$ is obtained by integrating the constitutive equations using $\dot{\boldsymbol{\varepsilon}}^\star = \mathbb{K} : \dot{\boldsymbol{\varepsilon}} + {}^1\!/_3\dot{\theta}\mathbf{1}$ as the strain rate and $\boldsymbol{\sigma} = \mathbb{K} : \boldsymbol{\sigma}^\star + p\mathbf{1}$. Furthermore, $\dot{\Pi}_e$ represents the power of external forces, and Ω denotes the entire body.

In the following, bracketed quantities ($\{\cdot\}$) represent vectors of nodal values. Following (Pinsky et al., 1983) and the implementation detailed in (Healy et al., 2020), a mid-increment scheme is used to obtain strains. The transformation gradients at mid-increment and end of increment are given by:

$$\boldsymbol{F}_{\frac{1}{2}} = \mathbf{1} + \boldsymbol{B}_F.\{\boldsymbol{u}\}_{\frac{1}{2}} \quad \boldsymbol{F} = \mathbf{1} + \boldsymbol{B}_F.\{\boldsymbol{u}\} \tag{23}$$

where $_{\frac{1}{2}}$ indicates quantities at mid-increment. Otherwise, quantities are taken at the end of the increment. The $\boldsymbol{B}_F$ matrix is computed using the derivatives of the quadratic shape functions. It only depends on the initial element coordinates, and is therefore constant. A polar decomposition is used to express the transformation gradients: $\boldsymbol{F}_{\frac{1}{2}} = \boldsymbol{R}_{\frac{1}{2}}.\boldsymbol{U}_{\frac{1}{2}}$ and $\boldsymbol{F} = \boldsymbol{R}.\boldsymbol{U}$. The strain increment over Δt is then obtained as:

$$\Delta\boldsymbol{\varepsilon} = \boldsymbol{B}_{\frac{1}{2}}.\left(\{\boldsymbol{u}\} - \{\boldsymbol{u}\}_0\right) = \boldsymbol{B}_{\frac{1}{2}}.\Delta\{\boldsymbol{u}\} \tag{24}$$

where $_0$ indicates quantities at the beginning of the increment. The matrix $\boldsymbol{B}_{\frac{1}{2}}$ is computed using the derivatives of the quadratic shape functions and the positions of nodes at mid-increment. The volume variation is computed from $\boldsymbol{\theta}$ using the linear shape functions as:

$$\theta = \boldsymbol{N}.\{\theta\} \qquad \Delta\theta = \boldsymbol{N}.\left(\{\theta\} - \{\theta\}_0\right) \tag{25}$$

where $\boldsymbol{N}$ is the vector of linear shape functions. The strain increment (eq. 24) is modified as:

$$\Delta\boldsymbol{\varepsilon}^{\star} = \mathbb{K} : \Delta\boldsymbol{\varepsilon} + \frac{1}{3}\Delta\theta\mathbf{1} \tag{26}$$

This deformation is then rotated in the material unrotated configuration as:

$$\Delta\boldsymbol{\varepsilon}^{\star\star} = \boldsymbol{R}^{T}_{\frac{1}{2}}.\Delta\boldsymbol{\varepsilon}^{\star}.\boldsymbol{R}_{\frac{1}{2}} \tag{27}$$

$\boldsymbol{\varepsilon}^{\star\star}$ is then used as the input strain for the constitutive equations, which provide the corresponding stress tensor $\boldsymbol{\sigma}^{\star\star}$, which is rotated to the end of the increment: $\boldsymbol{\sigma}^{\star} = \boldsymbol{R}.\boldsymbol{\sigma}^{\star\star}.\boldsymbol{R}^{T}$. Finally, the stress tensor corrected for pressure is computed as:

$$\boldsymbol{\sigma} = \mathbb{K} : \boldsymbol{\sigma}^{\star} + p\mathbf{1} \quad \text{with } p = \boldsymbol{N}.\{p\} \tag{28}$$

Considering eq. 22, the elementary forces corresponding to $\{\boldsymbol{u}\}$, $\{p\}$ and $\{\theta\}$ are obtained as:

$$\{F\}_{u} = \int_{\Omega_e} \boldsymbol{B}^{T}.\boldsymbol{\sigma}\, d\Omega \tag{29}$$

$$\{F\}_{p} = \int_{\Omega_e} (\text{trace}\Delta\boldsymbol{\epsilon} - \Delta\theta)\, \boldsymbol{N}\, d\Omega \tag{30}$$

$$\{F\}_{\theta} = \int_{\Omega_e} \left(\frac{1}{3}\text{trace}\boldsymbol{\sigma}^{\star} - p\right) \boldsymbol{N}\, d\Omega \tag{31}$$

where Ω_e represents the volume of the element at the end of the increment. The volume integration is performed using a standard Gauss method.

Using pressure at nodes, the pressure gradient can directly be computed as: $\boldsymbol{\nabla} p = \boldsymbol{G}.\{p\}$ where the matrix $\boldsymbol{G}$ is computed using the derivative of the linear shape functions and the nodal positions at the end of the increment. As described above, $\boldsymbol{\nabla} p$ is used as an input variable for the constitutive equations.

To prove the efficiency of the method, fig. 2 compares the pressure fields ahead of a blunted crack using the standard FE (displacement-based) and the proposed mixed formulation. Simulations are carried out using von Mises plasticity (the hardening law is given below in tab. 1). Strong pressure oscillations close to the blunted crack, where plastic strains are high, are observed using the standard formulation. They are eliminated using the mixed formulation.

4.4. Element formulation: nonlocal variables

For each nonlocal variable (with $\upsilon = \omega$ or κ), the weak form of eq. 9 and eq. 10 is expressed as follows, assuming the boundary conditions given by eq. 11 (El Ouazani Tuhami et al., 2022):

$$\int_{\Omega} \left[(\overline{\upsilon} - \upsilon)\overline{\upsilon}^{*} + l_{\upsilon}^{2}\boldsymbol{\nabla}\overline{\upsilon}.\boldsymbol{\nabla}\overline{\upsilon}^{*}\right] d\Omega = 0 \quad \forall\overline{\upsilon}^{*} \tag{32}$$

where υ^{*} is an arbitrary test function. The corresponding elementary force is then:

$$\{F\}_{\overline{\upsilon}} = \int_{\Omega_e} \left((\overline{\upsilon} - \upsilon)\boldsymbol{N} + l_{\upsilon}^{2}\boldsymbol{G}^{T}.\boldsymbol{G}.\{\overline{\upsilon}\}\right) d\Omega \quad \text{with } \overline{\upsilon} = \boldsymbol{N}.\{\overline{\upsilon}\} \tag{33}$$

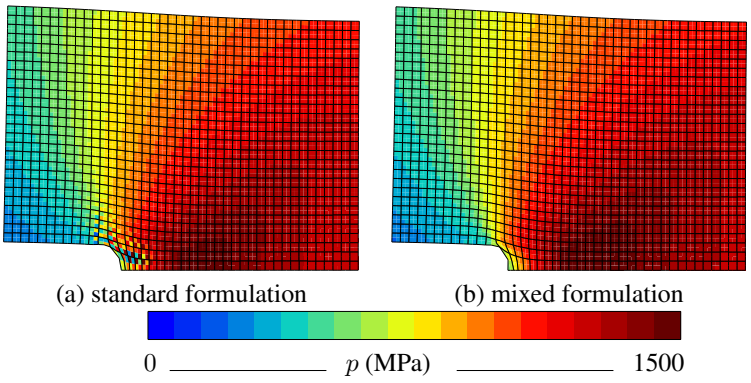

Figure 2:

Comparison of pressure fields using (a) standard FE formulation and using (b) the mixed formulation.

4.5. Element formulation: diffusion of lattice hydrogen

The conservation of hydrogen atoms is expressed as:

$$\frac{d}{dt}\int_V (C_L + C_T)\, dV + \int_{\partial V} \boldsymbol{J}.\boldsymbol{n}\, dS = 0 \tag{34}$$

Considering a volume V and its boundary ∂V, where $\boldsymbol{n}$ represents the outward normal to V. Following the approach in (Sofronis and McMeeking, 1989), it is assumed that the solid body's deformation has a negligible impact on diffusion.

This equation can then be rewritten in a local strong form using the divergence theorem and eq. 16 as:

$$(1 + H_{C_L})\dot{C}_L + h + \mathrm{div}(\boldsymbol{J}) = 0 \tag{35}$$

Multiplying this equation by an arbitrary test function C_L^* and integrating over the volume of the body leads to the weak form of the problem:

$$\int_\Omega \left[(1 + H_{C_L})\frac{dC_L}{dt}C_L^* + hC_L^* + \mathrm{div}(\boldsymbol{J})C_L^*\right] d\Omega = 0 \qquad \forall C_L^* \tag{36}$$

Noting that $\mathrm{div}(C_L^*\boldsymbol{J}) = \boldsymbol{\nabla} C_L^*.\boldsymbol{J} + C_L^*\mathrm{div}(\boldsymbol{J})$, eq. 36 can be rewritten as:

$$\int_\Omega \left[(1 + H_{C_L})\frac{dC_L}{dt}C_L^* + hC_L^* + \mathrm{div}(C_L^*\boldsymbol{J}) - \boldsymbol{\nabla} C_L^*.\boldsymbol{J}\right] d\Omega = 0 \qquad \forall C_L^* \tag{37}$$

or, using the divergence theorem:

$$\int_\Omega \left[(1 + H_{C_L})\frac{dC_L}{dt}C_L^* + hC_L^* - \boldsymbol{\nabla} C_L^*.\boldsymbol{J}\right] d\Omega + \int_{\partial\Omega} C_L^*\boldsymbol{J}.\boldsymbol{n}\, d\partial\Omega = 0 \qquad \forall C_L^* \tag{38}$$

This form can then be used to derive the finite element formulation of the problem. The concentration within the element is computed as $C_L = \boldsymbol{N}.\{C_L\}$ and its gradient as $\boldsymbol{\nabla} C_L = \boldsymbol{G}.\{C_L\}$ In eq. 38, dC_L/dt is approximated as:

$$\frac{dC_L}{dt} = \frac{1}{\Delta t}\boldsymbol{N}.\left(\{C_L\} - \{C_L\}_0\right) = \frac{1}{\Delta t}\boldsymbol{N}.\{\Delta C_L\} \equiv \frac{\Delta C_L}{\Delta t} \tag{39}$$

Finally, the elementary forces associated to $\{C_L\}$ are expressed as:

$$\{F\}_{C_L} = \int_{\Omega_e} \left[\left(\left(1 + H_{C_L}\right) \frac{\Delta C_L}{\Delta t} + h \right) \boldsymbol{N} - \boldsymbol{G}^T . \boldsymbol{J} \right] d\Omega \tag{40}$$

This generic form is also suitable for other cases involving diffusion, such as hydrogen diffusion in zirconium alloys with precipitation/dissolution of hydrides. In that particular case, $H_{C_L} = 0$ and h depends on the precipitation/dissolution kinetics.

At this point, the finite element formulation is fully defined. To obtain good convergence properties of the incremental resolution scheme, it is necessary to evaluate the elementary stiffness matrix (not detailed in this work), which is formally expressed as:

$$\boldsymbol{K} = \begin{pmatrix} \boldsymbol{K}_{uu} & \boldsymbol{K}_{up} & \cdots \\ \boldsymbol{K}_{pu} & \boldsymbol{K}_{pp} & \cdots \\ \cdots & \cdots & \ddots \end{pmatrix} \tag{41}$$

where the sub-matrices are calculated as: $\boldsymbol{K}_{uu} = \partial\{F\}_u / \partial\{u\}$, etc…

4.6. Boundary conditions for the diffusion problem

Dirichlet/Neumann boundary conditions are used to prescribe C_L or $\boldsymbol{J}$ on some parts of the boundaries of the body. In the case of an applied hydrogen pressure (P_a), the hydrogen concentration can be prescribed using Sieverts' law stating that (Sofronis and McMeeking, 1989):

$$C_L = C_S \sqrt{\frac{P_a}{P_S}} \tag{42}$$

where P_S is a reference pressure and C_S a thermally activated term. Prior to testing, the surface of the specimens is oxidized due to the exposition to the atmosphere before testing. Although small, the oxide layer may prevent or at least reduce the penetration of hydrogen in the material. The plastic deformation of the specimen will break this layer and allow hydrogen to diffuse into the material. To represent the interfacial resistance to hydrogen penetration in the material, the flux normal to the surface (J_n) can be expressed as (Robin boundary condition):

$$J_n = R_H (C_L^\infty - C_L) \tag{43}$$

where C_L^∞ is the equilibrium hydrogen concentration given by eq. 42 and C_L the concentration at the free surface (Kasuya et al., 2021). When $R_H \approx 0$, hydrogen penetration is blocked whereas, when R_H is large enough, $C_L \approx C_L^\infty$. To represent the cracking of the oxide layer, R_H is expressed as a function of $\overline{\kappa}$ and/or $\dot{\overline{\kappa}}$. In the FE implementation, it is important to consider the dependence of J_n on both C_L and $\overline{\kappa}$ to achieve good convergence. This boundary condition is not used in the following, but could be useful in other studies.

5. Simulation of an existing database

5.1. Database and material coefficients

The present study utilizes the database presented in (Briottet et al., 2012; Moro et al., 2010), which investigated the impact of gaseous hydrogen on the mechanical and fracture properties of a high-strength steel (API X80 grade) in an environment of hydrogen and neutral gas. To achieve this objective, a range of mechanical tests was performed, including tensile, fracture toughness with compact tension (CT) specimens and pressurized disk tests. All experiments were conducted at room temperature to ensure an accurate characterization of the material behavior under typical service conditions. Through these analyses, the mechanical and fracture properties of the material were fully characterized and the effect of hydrogen on these properties was determined.

To identify the material parameters for finite element simulation, the stress-strain curve of the smooth specimen was analyzed under nitrogen gas conditions, devoid of any embrittlement effect. The experimental data was fitted to the following equation:

$$R(\kappa) = R_0 + Q_1(1 - \exp(-b_1\kappa)) + Q_2(1 - \exp(-b_2\kappa)) \tag{44}$$

where R_0 denotes the yield stress, Q_1, b_1, Q_2, and b_2 represent the evolution of strain hardening, and κ is the accumulated plastic strain. Parameters representing the strain-rate sensitivity (eq. 5) of the material were also adjusted. The values of these parameters are presented in table 1. The initial porosity representing inclusions, such as MnS, CaS and oxides, is set to 4×10^{-4}. This relatively low value is representative of modern line pipe steels. q_1 was set to 1.5, as in other studies, and q_2 was adjusted so as to reproduce the experimental J–Δa curve of the material tested under air. Strain nucleation (A function in eq. 18) was also added to represent damage initiation on carbides (Tanguy et al., 2008). The effect of hydrogen on the nucleation on carbides is neglected, so $\zeta(C) = 1$. Parameters describing coalescence are set to $f_c = 0.05$, in agreement with results of unit cell simulations (Koplik and Needleman, 1988; Shinohara et al., 2016). Finally, $f_R = 0.25$ was used.

The nonlocal model requires the use of two internal lengths. The length for void growth was set, *a priori*, to 100 μm. This value corresponds to the size of the elements often used when modeling pipeline steels using a local model (see *e.g.* (Madi et al., 2020)). To account for the fact that the length scale for quasi-cleavage is likely to be smaller, l_κ was set to 30 μm. Following (El Ouazani Tuhami et al., 2022), the mesh size should be less than one-third of the material length, so the mesh size is 10 μm in areas where the fracture is expected to occur. A 30 μm mesh size can be used if failure by void growth is the main failure mechanism.

Experiments in (Briottet et al., 2012) did not evidence any effect of hydrogen on the overall plastic behavior, so that $\xi(C) = 1$ was chosen (eq. 17). For this reason, parameters q_1 and q_2 of the GTN model are kept constant. The applied hydrogen pressure was $P_a = 30$ MPa, which corresponds to a lattice hydrogen concentration equal to 4.4×10^{-3} wt. ppm (Moro et al., 2010). Using this information, Sieverts' law parameters at room temperature are evaluated (see tab. 1). The diffusion coefficient (D_L) at room temperature, the trap density (N_T) and the trap binding energy (W_B) are taken from (Moro et al., 2010). These parameters are also gathered in tab. 1. Note that different values can be found in the literature; for instance Depraetere et al. (2021) used $W_B = 60$ kJ/mol, $D_L = 1.5 \times 10^{-10}$ m^2/s and a different function for N_T ($\log_{10}(N_T) = 23.26 - 2.33\exp(-5.5\kappa)$ (at./m^3)) as in (Sofronis and McMeeking, 1989). All other parameters are well established and taken from (Sofronis and McMeeking, 1989).

In order to model hydrogen embrittlement, nucleation was added to the GTN model. As HE corresponds to quasi-cleavage, a stress dependence is introduced in the nucleation law. To reflect the deleterious effect of hydrogen on fracture resistance, the critical stress needed to trigger fracture is expressed as a function of the hydrogen concentration as:

$$\sigma_c = \sigma_c^0 \exp\left(-\frac{C}{C_0}\right) \tag{45}$$

where σ_c^0 and C_0 are material parameters. It is then assumed that the function expressing the nucleation rate due to quasi-cleavage (eq. 18) is expressed as:

$$B = \frac{B_0}{\sigma_c^0}\left\langle \sigma_I - (1 - q_1 f_\star)\sigma_c^0 \right\rangle \tag{46}$$

where $\langle\cdot\rangle$ denotes the positive part and B_0 is a material parameter. The critical stress is multiplied by $(1-q_1 f_\star)$ in the previous equation to account for the fact that σ_I decreases when damage increases. In the absence of this term, nucleation rapidly stops.

The number of parameters is high as the model proposes to describe ductile failure, hydrogen-induced quasi-brittle failure and the transition between both mechanisms in a unified framework. In this work, groups of parameters (see tab. 1) were identified separately. First, the elastoplastic behavior was fitted on tensile tests under N_2, assuming that damage remains negligible before the onset of rapid load drop. Then, the parameters describing ductile failure were fitted using test results in the absence of H_2. Finally, parameters describing hydrogen embrittlement were fitted using tests conducted under hydrogen. All parameters related to hydrogen diffusion were taken from the literature.

5.2. Tensile tests

Tensile tests were first simulated assuming no damage to investigate the coupling between mechanical loading and hydrogen diffusion and trapping. The sample's diameter is $\phi = 6$ mm and the gage length is 30 mm. Four calculations are performed. (i) The specimen is mechanically loaded under hydrogen pressure (30 MPa). (ii) The specimen is first precharged for one hour and then loaded. (iii) The specimen is first precharged, then loaded in air. In cases i—iii, the surface is assumed not to act as a diffusion barrier, so that the lattice concentration is prescribed at the surface (Dirichlet boundary conditions). In case (iii), this implies that the surface hydrogen lattice concentration drops to 0 as soon as the specimen is loaded and that hydrogen can escape from the material. (iv) The specimen is first precharged, then loaded assuming that hydrogen cannot escape (Neumann boundary conditions). The simulations are stopped when the maximum load is reached. All simulations were carried out with a strain rate equal to 5×10^{-5} s^{-1}. Only one-half of the axisymmetric specimen is meshed to account for symmetries. The material has an anisotropic behavior. In particular, the initially circular specimen cross-section deforms into an ellipse. This is a commonly observed behavior in pipeline steels (Tanguy et al., 2008; Shinohara et al., 2012). This effect is neglected in this study and the material is assumed to be isotropic. Accounting for anisotropy can be done by replacing the von Mises in eq. 2 by any anisotropic stress measure (Bron et al., 2004; Shinohara et al., 2016). In that case, a 3D simulation must be carried out.

Results of the various simulations are shown in fig. 3. In each case, C_L and C_T at the center (black lines) and close to the surface (red lines) on the symmetry plane are plotted as a function of

Property	Value	Unit
Mechanical behavior (plasticity and ductile damage)		
E, ν	209, 0.3	GPa, —
$\sigma_F(\kappa)$	$503 + 360(1 - \exp(-3.15\kappa))$ $+130(1 - \exp(-58.5\kappa))$	MPa
$\dot{\kappa}_0$, σ_0, n	1., 57., 5.3	s^{-1}, MPa, —
Ductile damage		
f_0	4.0×10^{-4}	—
q_1, q_2	1.5, 1.16	—
A	$A = 0$ if $\overline{\kappa} < 0.5$, $A = 0.1$ otherwise	—
f_c, f_R	0.05, 0.25	—, —
l_κ, l_ω	100., 100. or 30.	μm, μm
Hydrogen diffusion		
β	6	—
N_L	8.47×10^{28}	at/m^3
W_B	40	kJ/mol
R	8.31	J/mol K
T	300	K
N_T	$\log_{10}(N_T) = 24.73 - 3.74\exp(-60.17\overline{\kappa})$	at./m^3
D_L	1.27×10^{-8}	m^2/s
V_H	7.09×10^{-6}	m^3/mol
C_S, P_S	0.0129, 0.1013	at. ppm, MPa
Coupling		
$\xi(C)$, $\zeta(C)$	1, 1	—, —
σ_c^0, C_0, B_0	10200, 6.10 , 300	MPa, at. ppm, —

Table 1
Material parameters

time. C_T is also plotted at the stress concentration point (base of the fillet) in case iv. The distribution of C_T is given in each case at the end of the simulation ($t = 2700$ s corresponding to a deformation equal to 13.5%).

Considering the diameter of the specimen, the characteristic diffusion time in the absence of trapping is: $t_c = \phi^2/4D_L = 708$ s. Diffusion is, therefore, relatively fast compared to the duration of a tensile test. However, the trapping process and particularly the strong increase of the number of trapping sites during plastic deformation, results in the creation of a hydrogen-rich layer near the outer surface of the specimen (see fig. 3-(i)). This layer will therefore favor crack initiation from the surface, as experimentally evidenced in fig. 6 in (Moro et al., 2010). Precharging the specimen during one hour prior to testing (fig. 3-(ii)) allows for obtaining an initially uniform concentration within the specimen. However, the subsequent multiplication of trapping sites rapidly masks this effect, so that hydrogen distribution when reaching the maximum load is extremely close to that of case (i). In case (iii), hydrogen rapidly escapes from the specimen, resulting in an extremely low hydrogen concentration. This implies that hydrogen embrittlement would be avoided, provided that

the outer surface does not prevent hydrogen from escaping. In case (iv), the increase in the number of trapping sites leads to the increase of C_T and the decrease of C_L in the gauge length of the specimen. As pressure is higher at the root of the fillet, a slight hydrogen build-up is observed at this location. Since hydrogen is not allowed to enter, the material's overall concentration remains low. This implies that pre-charging (*e.g.* using electro-chemical charging) should reach higher concentrations of hydrogen levels to lead to similar embrittlement levels.

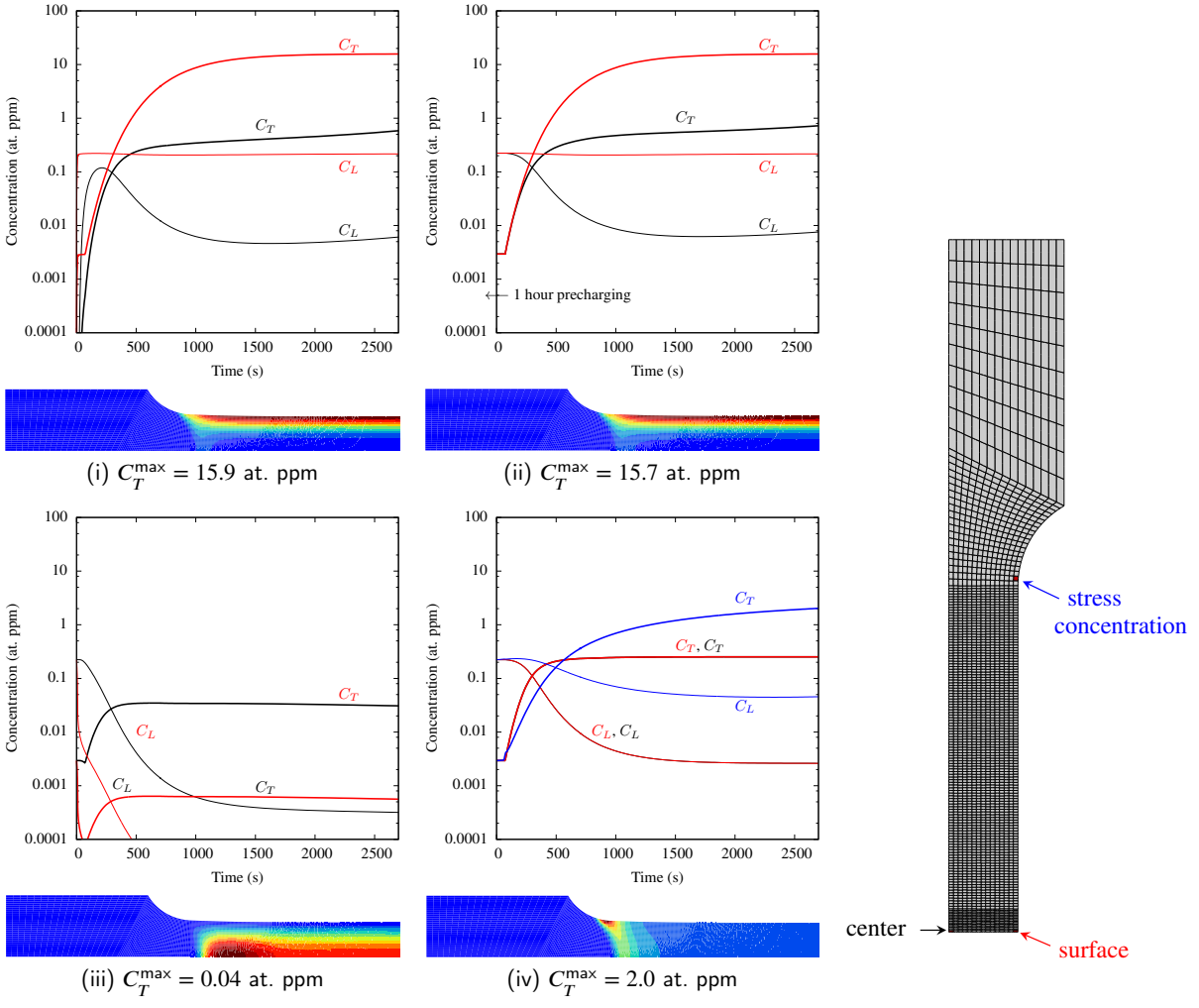

Figure 3: Simulation of a tensile test up to the maximum force assuming: (i) loading under hydrogen pressure, (ii) precharging and loading under hydrogen pressure, (iii) precharging and loading under air, (iv) precharging and loading assuming a tight surface. Curves indicate the hydrogen concentrations (C_L and C_T) in the element at the center of the specimen (black lines), in an element close to the outer surface (red lines) and in the stress concentration area (blue lines). The contour plots indicate the distribution of C_T at the end of the simulation.

The simulations are now conducted considering damage. The simulation results of tensile tests at various strain rates (5×10^{-7}, 5×10^{-5}, and 5×10^{-3} s^{-1}) are presented in fig. 4-(a) for case

(i) (indicated by black curves). The simulations qualitatively depict the influence of strain rate on ductility. At slow strain rates (5×10^{-7} s^{-1}), hydrogen has sufficient time to diffuse, leading to material embrittlement in the bulk. Consequently, damage is more pronounced at the center of the specimen where stresses are higher after the onset of necking. This is accompanied by a substantial loss of ductility. At a strain rate of 5×10^{-5} s^{-1}, crack initiation predominantly occurs from the surface, corroborating experimental findings by (Briottet et al., 2012). In contrast, the behavior of the specimen subjected to a strain rate of 5×10^{-3} s^{-1} closely resembles that of the specimen tested under nitrogen (indicated by the red curve). In that case, failure initiates at the center of the specimen due to ductile damage, but the load-carrying capacity is slightly reduced due to surface damage caused by hydrogen. Fig. 10-(b) illustrates the relationship between failure strain and strain rate for both numerical and experimental tests conducted under hydrogen conditions. The model successfully captures the observed strain rate effect up to a strain rate equal to 0.001 s^{-1}. Above this rate, the model overestimates ductility.

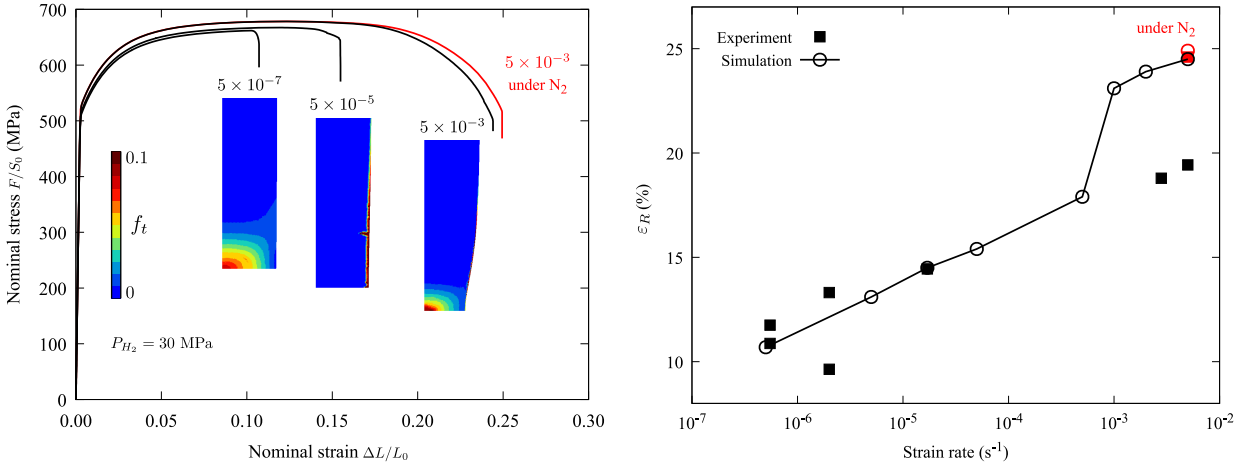

Figure 4: (a) Simulation of tensile tests at different strain rates under hydrogen. Damage maps are shown for strain rates equal to 5×10^{-7}, 5×10^{-5} and 5×10^{-3} s^{-1}. (b) Comparison between numerical and experimental data for the tensile test under hydrogen for different strain rates.

Fig. 5 closely examines damage development for a strain rate equal to 5×10^{-5} s^{-1}. As noted above, crack initiation occurs on the surface of the specimens due to a higher trapped hydrogen concentration in this region. Fig. 5-(a) illustrates the evolution of damage close to the surface for increasing nominal strains. Initially, damage uniformly increases in this region, but as the simulation progresses, multiple cracks form on the surface. This is similar to what was observed by Sicsic et al. (2014) using a gradient damage model to simulate thermal shocks. Both situations, however, strongly differ, but it is believed that the use of a nonlocal model enables to reproduce this effect. This eventually leads to the development of a main crack leading to final failure, as evidenced in the last figure. To examine the evolution of damage in the specimen, simulations of tensile tests conducted under hydrogen and nitrogen environments are compared for the same strain rate (5×10^{-5} s^{-1}). Fig. 5-(b) depicts the damage evolution at the center and surface of the specimen for both cases relative to the nominal strain. Significant differences are evidenced when comparing the two scenarios. When subjected to hydrogen, the surface experiences a gradual

increase in damage, resulting in surface cracking. Damage at the center of the specimen does not increase significantly. In contrast, during the test under nitrogen, the center of the specimen exhibits higher damage. It is worth noting that the void volume fraction reaches its peak at a lower strain in the hydrogen test, which is caused by the degradation caused by hydrogen, leading to premature failure.

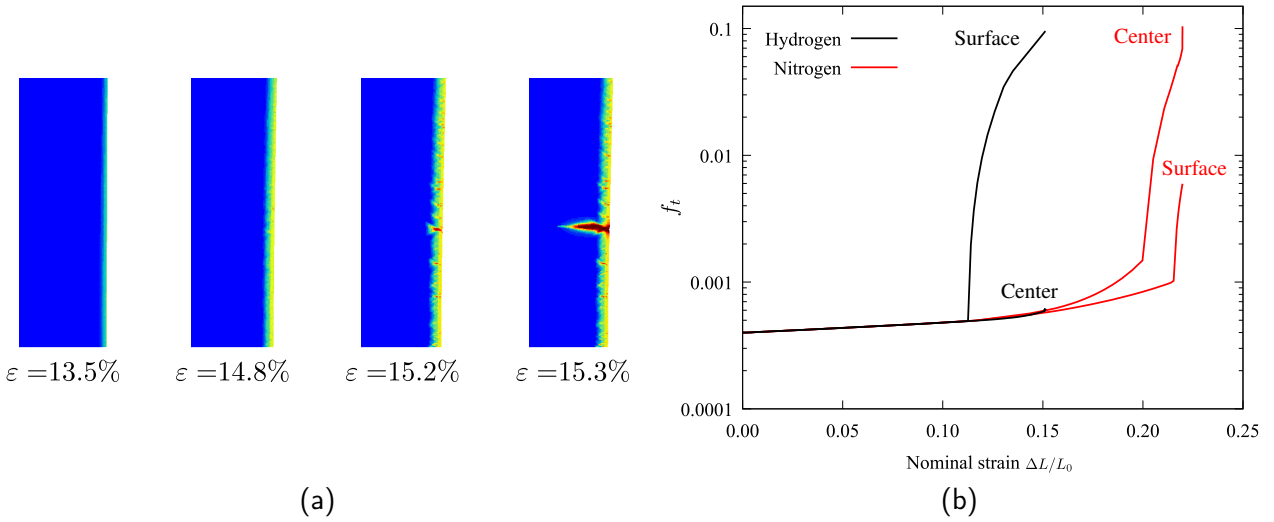

Figure 5: (a) Damage evolution on the surface of the tensile specimen in a H_2 environment. (b) Evolution of the total void volume fraction (f_t) as a function of nominal stress for tensile tests conducted under hydrogen and nitrogen environments. The tests were conducted at a strain rate of 5×10^{-5} s^{-1}.

5.3. Fracture toughness tests

Fracture toughness tests using compact tension (CT) specimens were conducted by (Briottet et al., 2012) with a loading rate equal to 0.1 mm/min under air and hydrogen under a pressure equal to 30 MPa. The geometry of the samples is presented in fig. 6-(a). Tests were conducted without side grooves using the multiple specimen technique of ASTM E1820. The specimen has a notch (20 mm deep) from which a fatigue pre-crack is inserted. The initial crack length is then $a_0 = 22$ mm.

Simulations are carried out assuming plane strain. One-half of the specimen is represented to account for symmetries. The mesh is shown in fig. 6-(b). As the crack propagates, it is important to impose the lattice hydrogen concentration derived from Sieverts' law on the newly formed crack. The corresponding boundary condition is applied to a node lying on the symmetry plane when one of the elements containing this node is considered broken (see detail in fig. 6-(b)). A similar technique was used in (del Bulto et al., 2017) together with cohesive elements to model crack advance. Another solution would be to strongly increase the diffusion coefficient in highly damaged regions or to use a penalty method, so that C_L quickly equals the prescribed concentration (Martínez-Pañeda et al., 2020).

The crack length was obtained by post-processing the simulation considering broken elements defined as elements for which all Gauss points have reached $f_\star = 0.99/q_1$. J is then computed using the ASTM E1820 standard considering the simulated Load–CMOD curve. Before crack initiation, the crack advance Δa is set to $\frac{1}{2}J/\sigma_Y$ to account for crack blunting because it is not

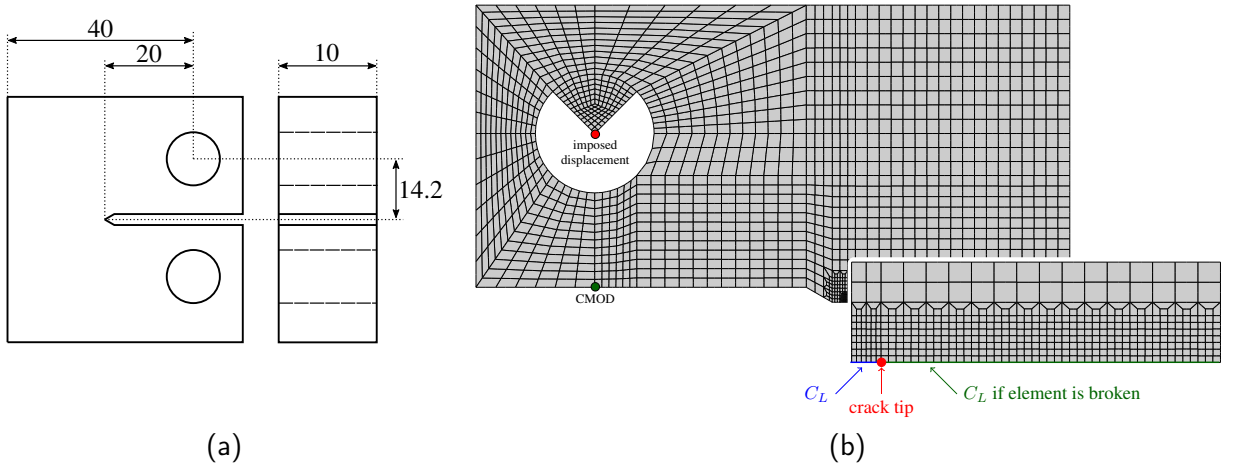

Figure 6: (a) Geometry of the compact tension specimen. (b) Specific boundary conditions for the lattice hydrogen concentration.

accounted for when only considering broken elements (see also (Chen et al., 2022)). $\sigma_Y = 590$ MPa is the average of the 0.2% proof stress and the Ultimate Tensile Stress.

The simulated J–Δa curves under air and hydrogen are plotted in fig. 7. A very good agreement with test results under air is obtained. The simulation still overestimates the J values obtained under hydrogen but a drastic drop in toughness is nevertheless obtained. Using a smaller value for l_κ could possibly solve this problem, leading to a much higher computational cost.

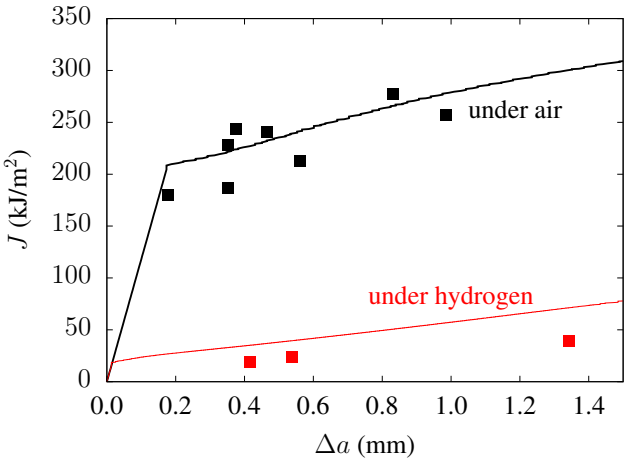

Figure 7: Simulated J–Δa curves. Lines: simulations. Symbols: experimental data from (Briottet et al., 2012).

Fig. 8 displays the values of the opening stress (σ_{22}) and the nonlocal accumulated plastic strain. Results indicate that the stress field does not present any spurious fluctuations thanks to the use of the mixed formulation. In addition, the strain is not localized due to the nonlocal formulation. As expected, the damage process zone (corresponding to the high-stress region ahead of the crack tip) is larger in the case of the CT tested under air.

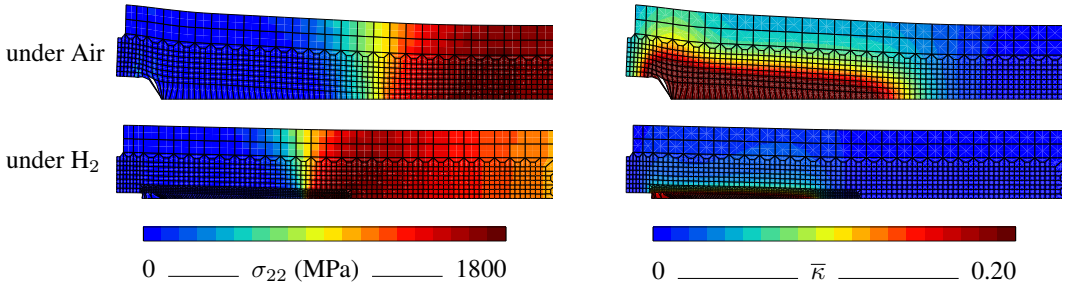

Figure 8: Values of the opening stress σ_{22} and $\overline{\kappa}$ at Gauss points for CT specimens tested under air and hydrogen. A finer mesh is used (10 μm) for tests under hydrogen to discretize the smaller length scale.

5.4. Pressurized disk tests

Assessing materials for hydrogen storage is crucial to ensure the safety and reliability of hydrogen storage applications. To this end, pressurized disk tests can be utilized for material qualification, following the ISO standard 11114-4 (ISO 11114-4, 2005). The test is designed to provide a reliable means of evaluating materials for hydrogen storage, ensuring that only materials capable of withstanding the high-pressure environments associated with hydrogen storage are utilized. The testing procedure involves subjecting a clamped disk to increasing pressures of helium or hydrogen gas (see fig. 9). The embrittlement ratio I_E is then calculated as the ratio of failure pressures in helium and hydrogen at a given pressure rate. A ratio of less than 2 is considered acceptable for hydrogen storage material.

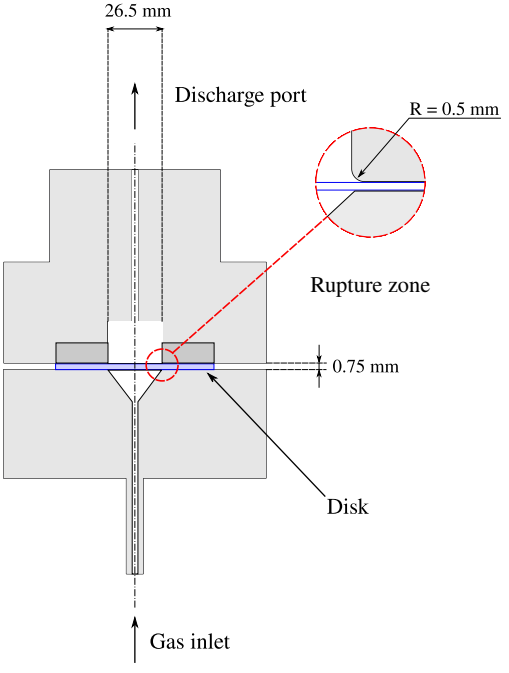

Figure 9: Representation of the machine used for the pressurized disk test.

According to the ISO standard, the pressurized disk test is performed using a 58 mm diameter disk with a thickness of 0.75 mm. The disk is clamped so that pressure is applied on a surface having

a diameter equal to 26.5 mm. The pressure is applied on one side. On the other side, the clamping device has a radius equal to 0.5 mm to avoid indentation of the disk (see fig. 9). A simulation of the test was proposed by Charles et al. (2012) using a cohesive zone model in the failure zone.

The rupture pressure of a disk at different pressurization rates, under helium and hydrogen gases, was investigated by Briottet et al. (2012). It was found that when the disk was exposed to helium, the rupture pressure was approximately 60 MPa. In contrast, when the disk was exposed to hydrogen, the rupture pressure ranged from 20 to 50 MPa. This reduction in rupture pressure was attributed to the hydrogen embrittlement effect, wherein hydrogen diffused within the material and caused it to become less ductile or brittle. Furthermore, it was found that the extent of hydrogen embrittlement was dependent on the pressurization rate; lower rates resulted in a more significant embrittlement effect due to increased hydrogen diffusion time.

For the numerical simulation, an axisymmetric mesh was employed. Contact between the disk and the upper clamping device is modeled assuming no friction. As the simulation is carried out for increasing pressure, it gets unstable and it diverges at the moment where rupture takes place. It was checked that the divergence corresponds to high levels of strain and damage. As the problem is time-dependent (due to the rate dependence of the material and diffusion), it is not possible to use an arc-length method (Riks, 1979) to control loading. In the case of simulations with hydrogen gas, the lattice concentration is prescribed on the pressurized side following Sieverts' law. On the other side, the condition $C_L = 0$ is used so that hydrogen can escape from the specimen. In practice, using a Neumann boundary condition (with $J_n = 0$) does not change the results, as failure always occurs on the pressurized side in the clamping area.

The results of the simulations are depicted in fig. 10, where the curve represents the displacement at the center of the disk vs. the gas pressure for a pressurization rate of $\dot{P} = 0.25$ MPa/min. It is observed that for both the test under helium and hydrogen, the rupture pressure is close to the experimental results found by Briottet et al. (2012). Both curves follow the same path, as hydrogen is assumed not to affect the hardening of the material. However, rupture takes place at a lower pressure under hydrogen. The simulations show that failure under helium is mainly because the limit load of the disk is reached when a strong reduction in thickness occurs near the clamping area. Simulations with and without damage lead to very similar failure pressures. Under hydrogen pressure, failure is caused by damage nucleation induced by local hydrogen uptake as shown in fig. 10, where the hydrogen concentrations C and C_L are displayed for the failure pressure. The accumulated plastic strain $\overline{\kappa}$ is also shown, indicating rupture in the clamping area.

The current study also explores how the pressurization rate influences disk failure. Various pressurization rates are applied to analyze their impact on hydrogen diffusion and the embrittlement effect. It was found that the small pressurization rates ($\dot{P}$) lead to a pronounced embrittlement caused by hydrogen, as it has a longer time to diffuse in the material. The results of this analysis are presented in fig. 11. They show a good agreement with the data reported in (Briottet et al., 2012). Note, however, that experimental results exhibit a large scatter. This could be because failure occurs in the clamping area, where boundary conditions are more difficult to control experimentally. A solution could be the use of notches machined in the disk away from the clamping zone, as proposed in (Moro, 2009; Lopes Pinto et al., 2022).

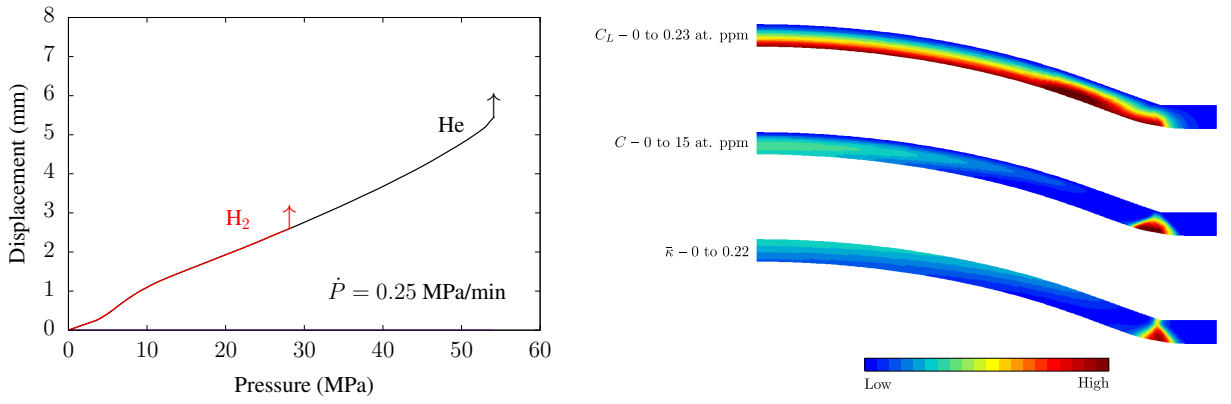

Figure 10: (a) Displacement at the center of the disk vs. the gas pressure under helium and hydrogen at a pressurization rate of $\dot{P} = 0.25$ MPa/min. (b) Contour plots for C_L, C and $\bar{\kappa}$ at instability for a test under H_2.

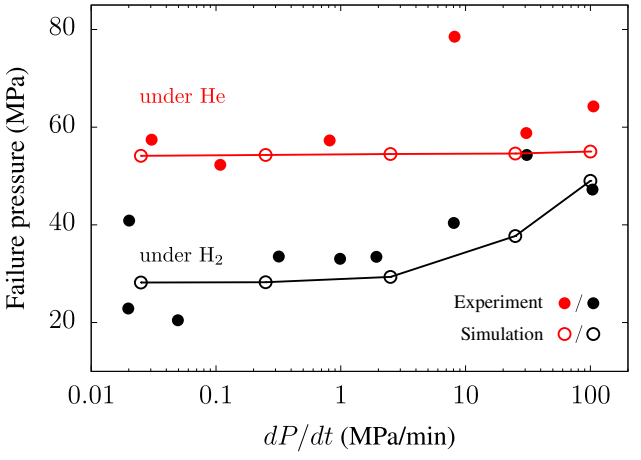

Figure 11: Rupture pressure for different pressurization rates under hydrogen and helium.

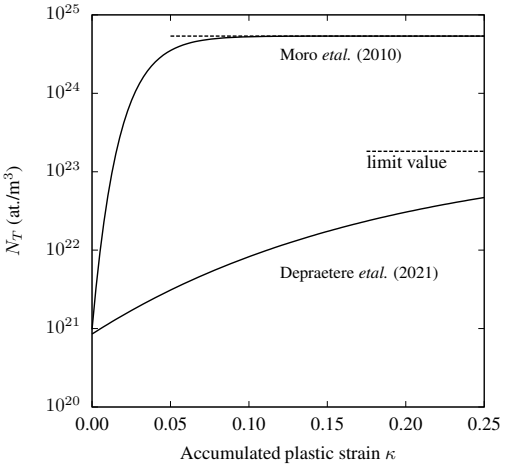

Figure 12: Comparison of the values of N_T in (Moro et al., 2010) and (Depraetere et al., 2021).

6. Discussion: effect of material parameters related to diffusion

As mentioned above, material parameters W_B, N_T and D_L proposed by Depraetere et al. (2021) and Moro et al. (2010) strongly differ, although the investigated materials appear to be very similar: X70 pipeline steel in the first case and X80 in the second case. To investigate the effect of these material parameters, the simulations of tensile tests presented in fig. 3 were performed using the set of parameters proposed in (Depraetere et al., 2021): $W_B = 60$ kJ/mol, $\log_{10}(N_T) = 23.26 - 2.33\exp(-5.5\overline{\kappa})$ (at./m^3) and $D_L = 1.5\,10^{-10}$ m^2/s. The values of N_T are compared in fig. 12. Values for $\overline{\kappa} = 0$ are very similar but strongly differ for increasing accumulated plastic strain. Values proposed in Moro et al. (2010) increase much faster with plastic strain and rapidly reach a higher limit value. The characteristic diffusion time is also increased, as D_L is much smaller in (Depraetere et al., 2021): $t_c = 60$ ks. All other parameters are kept constant, in particular the boundary conditions.

The four cases investigated in section 5.2 were simulated with the new set of parameters. Results are shown in fig. 13. For case (i), *i.e.* loading under hydrogen pressure, the hydrogen concentration is higher close to the specimen surface as in fig. 3. However, in that case, this is due to the slow diffusion into the material whereas, it is mainly due to trapping in the other case. As a result, the hydrogen concentration is also reduced (0.39 vs. 16 at. ppm). This implies that different nucleation parameters (eq. 7 and 45) should be used to describe ductility reduction in tension. One hour precharging does not significantly modify the results, as in section 5.2.

Due to the low diffusion coefficient, hydrogen hardly escapes from the specimen in case (iii). This result is consistent with the conclusions of Depraetere et al. (2021). This implies that hydrogen embrittlement should still be evidenced in that case whereas it is likely to vanish using the parameters from Briottet et al. (2012). This could be a way to discriminate hypotheses on boundary conditions. If the specimen is assumed to be tight (case iv), hydrogen redistribution does not occur in the specimen, contrary to the results presented in section 5.2. Once more, this is due to the significantly smaller diffusion coefficient.

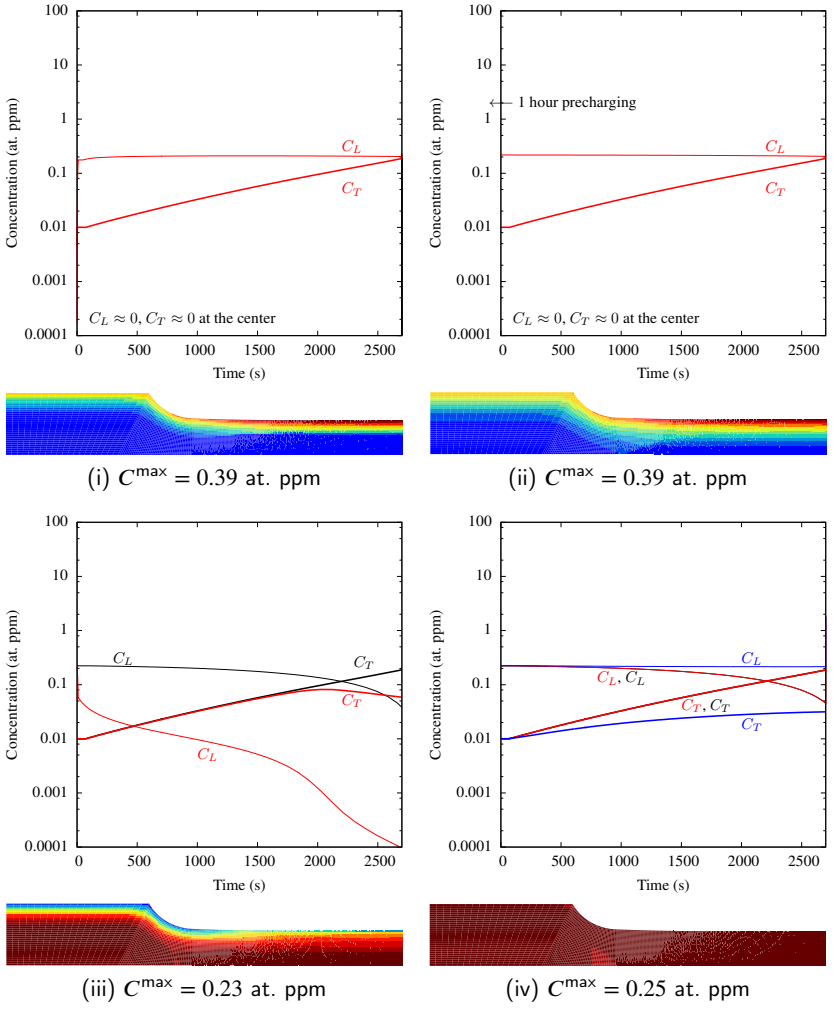

(i) $C^{\max} = 0.39$ at. ppm (ii) $C^{\max} = 0.39$ at. ppm

(iii) $C^{\max} = 0.23$ at. ppm (iv) $C^{\max} = 0.25$ at. ppm

Figure 13: Simulation of a tensile test for diffusion parameters given in (Depraetere et al., 2021) up to the maximum force assuming: (i) loading under hydrogen pressure, (ii) precharging and loading under hydrogen pressure, (iii) precharging and loading under air, (iv) precharging and loading assuming a tight surface. Curves indicate the hydrogen concentrations (C_L and C_T) in the element at the center of the specimen (black lines), in an element close to the outer surface (red lines) and in the stress concentration area (blue lines). The contour plots indicate the distribution of C at the end of the simulation.

7. Conclusions

This paper presents a numerical framework for simulating hydrogen embrittlement using a modified nonlocal Gurson-Tvergaard-Needleman (GTN) model coupled with hydrogen diffusion. In this model, the evolution of damage is accelerated by the hydrogen concentration to represent HEDE, leading to premature failure under hydrogen. To overcome issues such as volumetric locking and to obtain continuous pressure fields, a mixed formulation incorporating displacement, pressure, and volume variation is employed. This formulation uses pressure as a nodal variable. This allows the straightforward calculation of the pressure gradient which strongly influences hydrogen diffusion. Furthermore, the adoption of an implicit gradient model renders the model mesh-independent, allowing for the regularization of void growth and strain-controlled nucleation. The implementation of the model was carried out in the commercial software Z-SET.

To validate the model, calibration and testing were performed using experiments reported in (Moro et al., 2010; Briottet et al., 2012) on a high-strength steel of grade API X80. The experimental database consists of a series of tests including tensile tests, fracture toughness and pressurized disk tests.

The simulation of tensile tests allows modeling failure initiation from the surface of the specimen at low strain rates and the transition to failure initiation at the center of the specimen after necking at high strain rates. Tests on CT specimens are also successfully simulated as the proposed model can represent the drastic toughness reduction under hydrogen. Finally, the pressurized disk test is also well described by the model. In particular, the effect of the loading rate is well reproduced. It is suggested to use disk specimens with notches to avoid failure in the clamping area.

As the model attempts to simultaneously capture ductile fracture, quasi-cleavage induced by hydrogen as well as a seamless transition between both mechanisms, it introduces many material parameters. Fitting is, therefore, challenging. A step-by-step fitting procedure is proposed to ease identification. Parameters used to model quasi-cleavage (σ_c^0, C_0 and B_0) strongly affect the results. Note that alternative forms for the quasi-cleavage damage rule could be easily implemented within the proposed framework. These parameters also strongly depend on the parameters chosen to represent hydrogen diffusion and interaction with trapping sites. In this work, the parameters proposed by Moro et al. (2010) were employed; however, the utilization of those suggested in (Depraetere et al., 2021) would have resulted in very different values for σ_c^0, C_0, and B_0.

This study used an *ad hoc* boundary condition to represent the penetration of the gaseous hydrogen into newly opened cracks. An improved solution would be to use re-meshing to explicitly represent cracks as in (Mediavilla et al., 2006; El Ouazani Tuhami et al., accepted). The boundary conditions could then be applied to the newly created crack lips. In addition, re-meshing can be used to propagate cracks over large distances while keeping the size of the problem constant by using a fine mesh only in the fracture process zone.

Acknowledgments: This work is funded by the ANR Chair program Messiah (ANR-20-CHIN-0003)

References

Abbasi, S., 2011. 'Renewable' hydrogen: Prospects and challenges. Renewable and Sustainable Energy Reviews 6, 3034–3040.
Ahn, D., Sofronis, P., Dodds, R.J., 2007. Modeling of hydrogen-assisted ductile crack propagation in metals and alloys. Int. J. Frac. 145, 135–157.

Ambati, M., Gerasimov, T., De Lorenzis, L., 2015. Phase-field modeling of ductile fracture. Comput. Mech. 55, 1017–1040.

Barnoush, A., Vehoff, H., 2010. Recent developments in the study of hydrogen embrittlement: hydrogen effect on dislocation nucleation. Acta Mater. 58, 5274–5285.

Bazant, Z., Pijaudier-Cabot, G., 1988. Non local continuum damage. localization, instability and convergence. J. Applied Mech. 55, 287–294.

Beachem, C., 1972. A new model for hydrogen-assisted cracking (hydrogen 'embrittlement'). Met. Trans. 3, 441–455.

Bellet, M., 1999. Finite element analysis of compressible viscoplasticity using a three-field formulation. application to metal powder hot compaction. Comp. Meth. Appl. Mech. Engng 175, 19–40.

Benannoune, S., Charles, Y., Mougenot, J., Gasperini, M., De Temmerman, G., 2019. Numerical simulation by finite element modelling of diffusion and transient hydrogen trapping processes in plasma facing components. Nucl. Mater. Energy 19, 42–46.

Besson, J., Foerch, R., 1997. Large scale object–oriented finite element code design. Comp. Meth. Appl. Mech. Engng 142, 165–187.

Besson, J., Steglich, D., Brocks, W., 2001. Modeling of crack growth in round bars and plane strain specimens. Int. J. Solids Structures 38, 8259–8284.

Brepols, T., Wulfinghoff, S., Reese, S., 2017. Gradient-extended two-surface damage-plasticity: Micromorphic formulation and numerical aspects. Int. J. Plasticity 97, 64–106.

Briottet, L., Moro, I., Lemoine, P., 2012. Quantifying the hydrogen embrittlement of pipeline steels for safety considerations. Int. J. Hydrog. Energy 37, 17616–17623.

Bron, F., Besson, J., Pineau, A., 2004. Ductile rupture in thin sheets of two grades of 2024 aluminum alloy. Mater. Sci. Engng A 380, 356–364.

del Bulto, S., Betegón, C., Martínez-Pañeda, E., 2017. A cohesive zone framework for environmentally assisted fatigue. Eng. Fract. Mech. 185, 210–226.

Charles, Y., Gaspérini, M., Disashi, J., Jouinot, P., 2012. Numerical modeling of the Disk Pressure Test up to failure under gaseous hydrogen. J. Mater. Processing Technol. 212, 1761–1770.

Chen, Y., Lorentz, E., Besson, J., 2020. Properties of a nonlocal GTN model within the context of small—scale yielding. Int. J. Plasticity , 102701.

Chen, Y., Lorentz, E., Dahl, A., Besson, J., 2022. Simulation of ductile tearing during a full size test using a non local Gurson-Tvergaard-Needleman (GTN) model. Eng. Fract. Mech. 216, 108226.

Chu, C., Needleman, A., 1980. Void nucleation effects in biaxially stretched sheets. J. Engng Mater. Technol. 102, 249–256.

Dalloz, A., Besson, J., Gourgues-Lorenzon, A.F., Sturel, T., Pineau, A., 2009. Effect of shear cutting on ductility of a dual phase steel. Eng. Fract. Mech. 76, 1411–1424.

Depraetere, R., De Waele, W., Hertelé, S., 2021. Fully-coupled continuum damage model for simulation of plasticity dominated hydrogen embrittlement mechanisms. Comput. Mat. Sci. 200, 110857.

Diamantopoulou, E., Liu, W., Labergere, C., Badreddine, H., Saanouni, K., Hu, P., 2017. Micromorphic constitutive equations with damage applied to metal forming. Int. J. Damage Mech. 26, 314–339.

Dittmann, M., Aldakheel, F., Schulte, J., Schmidt, F., Krüge, M., Wriggers, P., Hesch, C., 2020. Phase-field modeling of porous-ductile fracture in non-linear thermo-elasto-plastic solids. Comp. Meth. Appl. Mech. Engng 361, 112730.

El Ouazani Tuhami, A., Feld-Payet, S., Quilici, S., Osipov, N., Besson, J., accepted. Simulations of complex crack paths using a robust and cost-efficient continuous-discontinuous approach. Int. J. Solids Structures doi:10.1016/j.ijsolstr.2023.112199.

El Ouazani Tuhami, A., Feld-Payet, S.a nd Quilici, S., Osipov, N., Besson, J., 2022. A two characteristic length nonlocal GTN model: Application to cup-cone and slant fracture. Mech. Mater. 171, 104350.

Eldahshan, H., Bouchard, P.O., Alves, J., Perchat, E., Pino Munoz, D., 2021. Phase field modeling of ductile fracture at large plastic strains using adaptive isotropic remeshing. Computational Mechanics 67, 763–783.

Enakoutsa, K., Leblond, J., Perrin, G., 2007. Numerical implementation and assessment of a phenomenological nonlocal model of ductile rupture. Comp. Meth. Appl. Mech. Engng 196, 1946–1957.

Faleskog, J., Gao, X., Shih, C., 1998. Cell model for nonlinear fracture analysis — I. Micromechanics calibration. Int. J. Frac. 89, 355–373.

Ferreira, P., Robertson, I., Birnbaum, H., 1999. Hydrogen effects on the character of dislocations in high-purity aluminium. Acta Metall. 47, 2991–2998.

Foerch, R., Besson, J., Cailletaud, G., Pilvin, P., 1997. Polymorphic constitutive equations in finite element codes. Comp. Meth. Appl. Mech. Engng 141, 355–372.

Forest, S., 2009. Micromorphic approach for gradient elasticity, viscoplasticity, and damage. J. Eng. Mech. 135, 117–131.

Gerberich, W., Marsh, P., Hoehn, J., 1994. Hydrogen Induced Cracking Mechanisms — Are There Critical Experiments?. John Wiley & Sons, Ltd. pp. 539–554.

Healy, B., Gullerud, A., Koppenhoefer, K., Roy, A., RoyChowdhury, S., Petti, J., Walters, W., Bichon, B., Cochran, K., Carlyle, A., Sobotka, J., Messner, M., Truster, T., Dodds, R., 2020. WARP3D-Release 18.2.1 3-D Dynamic Nonlinear Fracture Analyses of Solids Using Parallel Computers. Technical Report. University of Illinois at Urbana-Champaign.

Hirth, J., 1980. Effects of hydrogen on the properties of iron and steel. Met. Trans. A 11A, 861–890.

Huespe, A.E., Needleman, A., Oliver, J., Sánchez, P.J., 2009. A finite thickness band method for ductile fracture analysis. Int. J. Plasticity 25, 2349–2365.

Hütter, G., Linse, T., Mühlich, U., Kuna, M., 2013. Simulation of ductile crack initiation and propagation by means of a non-local Gurson-model. Int. J. Solids Structures 50, 662–671.

ISO 11114-4, 2005. ISO/FDIS 11114-4:2005(E) Transportable gas cylinders — Compatibility of cylinder and valve materials with gas contents — Part 4: Test methods for selecting metallic materials resistant to hydrogen embrittlement. Technical Report.

Javani, H., Peerlings, R., Geers, M., 2016. Three-dimensional finite element modeling of ductile crack initiation and propagation. Adv. Model. and Simul. in Eng. Sci. , 3–19.

Jemblie, L., Olden, V., Akselsen, O., 2017. A coupled diffusion and cohesive zone modelling approach for numerically assessing hydrogen embrittlement of steel structures. Int. J. Hydrogen Energy 42, 11980–11995.

Kasuya, T., Yokobori, A., Ozeki, G., Ohmi, T., Enoki, M., 2021. Modelling of hydrogen diffusion in a weld cold cracking test: Part 1, experimental determinations of apparent diffusion coefficient and boundary condition. ISIJ Int. 61, 1245–1253.

Koplik, J., Needleman, A., 1988. Void growth and coalescence in porous plastic solids. Int. J. Solids Structures 24, 835–853.

Krom, A., Koers, R., Bakker, A., 1999. Hydrogen transport near a blunting crack tip. J. Mech. Phys. Solids 47, 971–992.

Leclerc, J., Nguyen, V., Pardoen, T., Noels, L., 2020. A micromechanics-based non-local damage to crack transition framework for porous elastoplastic solids. Int. J. Plasticity 127.

Lin, M., Yu, H., Ding, Y., Olden, V. ans Alvaro, A., He, J. annd Zhang, Z., 2022a. Simulation of ductile-to-brittle transition combining complete gurson model and czm with application to hydrogen embrittlement. Eng. Fract. Mech. 268, 108511.

Lin, M., Yu, H., Ding, Y., Wang, G., Olden, V., Alvaro, A., He, J., Zhang, Z., 2022b. A predictive model unifying hydrogen enhanced plasticity and decohesion. Scr. Mater. 215.

Linse, T., Hütter, G., Kuna, M., 2012. Simulation of crack propagation using a gradient-enriched ductile damage model based on dilatational strain. Eng. Fract. Mech. 95, 13–28.

Lopes Pinto, D., Madi, Y., Lacourt, L., Osipov, N., Quilici, S., El Ouazani Tuhami, A., Furtado, J., Gallienne, N., Besson, J., 2022. Study of hydrogen embrittlement in steels using pressurized disks, in: Proceedings of the Fourth International Conference on Metals & Hydrogen, p. 11.

Madi, Y., Shinohara, Y., Besson, J., 2020. Effect of prestrain on ductility and toughness in a high-strength line pipe steel. Int. J. Frac. 224, 15–29.

Martínez-Pañeda, E., Golahmar, A., Niordson, C., 2018. A phase field formulation for hydrogen assisted cracking. Comp. Meth. Appl. Mech. Engng 342, 742–761.

Martínez-Pañeda, E., Harris, Z., Fuentes-Alonso, S., Scully, J., Burns, J., 2020. On the suitability of slow strain rate tensile testing for assessing hydrogen embrittlement susceptibility. Corrosion Science 163, 108291.

Martínez-Pañeda, E., Niordson, C., Gangloff, R., 2016. Strain gradient plasticity-based modeling of hydrogen environment assisted cracking. Acta Mater. 117, 321–332.

Mediavilla, J., Peerlings, R., Geers, M., 2006. Discrete crack modelling of ductile fracture driven by non-local softening plasticity. Int. J. Numer. Meth. Engng 66, 661–688.

Mediavilla, J., Peerlings, R., Geers, M., 2006. A nonlocal triaxiality-dependent ductile damage model for finite strain plasticity. Comp. Meth. Appl. Mech. Engng 195, 4617–4634.

Mediavilla, J., Peerlings, R., Geers, M., 2006. A robust and consistent remeshing-transfer operator for ductile fracture simulations. Computers & Structures 84, 604–623.

Meibom, P., Karlsson, K., 2010. Role of hydrogen in future North European power system in 2060. Int. J. Hydrog. Energy 35, 1853–1863.

Miehe, C., Aldakheel, F., Raina, A., 2016. Phase field modeling of ductile fracture at finite strains: A variational gradient-extended plasticity-damage theory. Int. J. Plasticity 84, 1–32.

Moro, I., 2009. Fragilisation par l'hydrogène gazeux d'un acier ferrito-perlitique de grade API X80. Ph.D. thesis. Université Toulouse III - Paul Sabatier.

Moro, I., Briottet, L., Lemoine, P., Andrieu, E., Blanc, C., Odemer, G., 2010. Hydrogen embrittlement susceptibility of a high strength steel X80. Mater. Sci. Engng A 527, 7252–7260.

Nagumo, M., 2004. Hydrogen related failure of steels – a new aspect. Materials Science and Technology 20, 940–950. doi:10.1179/026708304225019687.

Nagumo, M., Nakamura, M., Taka, K., 2001. Hydrogen thermal desorption relevant to delayed-fracture susceptibility of high-strength steels. Metallurgical and Materials Transactions A 32, 339–347.

Olden, V., Thaulow, C., Johnsen, R., Østby, E., Berstad, T., 2008. Application of hydrogen influenced cohesive laws in the prediction of hydrogen induced stress cracking in 25steel. Eng. Fract. Mech. 75, 2333–2351.

Oriani, R., 1970. The diusion and trapping of hydrogen in steel. Acta Metall. 18, 147–157.

Peerlings, R., De Borst, R., Brekelmans, W., De Vree, J., Spee, I., 1996. Some observations on localisation in non–local and gradient damage models. Eur. J. Mech./A 15A.

Peerlings, R., Poh, L., Geers, M., 2012. An implicit gradient plasticity-damage theory for predicting size effects in hardening and softening. Eng. Fract. Mech. 95, 2–12.

Petit, T., Besson, J., Ritter, C., Colas, K., Helfen, L., Morgeneyer, T., 2019. Effect of hardening on toughness captured by stress-based damage nucleation in 6061 aluminum alloy. Acta Mater. 180, 349–365.

Pijaudier-Cabot, G., Bazant, Z.P., 1987. Nonlocal damage theory. J. Engrg. Mech. 113, 1512–1533.

Pinsky, P., Ortiz, M., Pister, K., 1983. Numerical integration of rate constitutive equations in finite deformation analysis. Comp. Meth. Appl. Mech. Engng 40, 137–158.

Rice, J., 1976. The localisation of plastic deformation, in: Koiter, W. (Ed.), Proc. 14th Int. Conf. Theoretical and Applied Mechanics, Delft, North–Holland, Amsterdam. pp. 207–220.

Riks, E., 1979. An incremental approach to the solution of snapping and buckling problems. Int. J. Solids Structures 15, 529–551.

Robertson, I., Sofronis, P., Nagao, A., Martin, M., Wang, S., Gross, D., Nygren, K., 2015. Hydrogen embrittlement understood. Metall. Mater. Trans. B 46B, 1085–1103.

Rudnicki, J., Rice, J., 1975. Conditions for the localization of deformation in pressure–sensitive dilatant materials. J. Mech. Phys. Solids 23, 371–394.

Scherer, J.M., Phalke, V., Besson, J., Forest, S., Hure, J., Tanguy, B., 2020. Lagrange multiplier based vs micromorphic gradient-enhanced rate-(in)dependent crystal plasticity modelling and simulation. Comp. Meth. Appl. Mech. Engng 372, 113426.

Seupel, A., Hütter, G., Kuna, M., 2020. On the identification and uniqueness of constitutive parameters for a non-local GTN-model. Eng. Fract. Mech. 229, 106817.

Shibata, A., Yonemura, T., Momotani, Y., Park, M.H., Takagi, S., Madi, Y., Besson, J., Tsuji, N., 2021. Effects of local stress, strain, and hydrogen content on hydrogen-related fracture behavior in low-carbon martensitic steel. Acta Mater. 210, 116828.

Shinohara, Y., Besson, J., Madi, Y., 2012. Anisotropic damage behavior in high-strength line pipe steels. Int. J. Offshore Polar Eng. 22, 83–89.
Shinohara, Y., Madi, Y., Besson, J., 2016. Anisotropic ductile failure of a high-strength line pipe steel. Int. J. Frac. 197, 127–145.
Sicsic, P., Marigo, J.J., Maurini, C., 2014. Initiation of a periodic array of cracks in the thermal shock problem: A gradient damage modeling. J. Mech. Phys. Solids 63, 256–284.
Sofronis, P., McMeeking, R., 1989. Numerical analysis of hydrogen transport near a blunting crack tip. J. Mech. Phys. Solids 37, 317–350.
Taha, A., Sofronis, P., 2001. A micromechanics approach to the study of hydrogen transport and embrittlement. Eng. Fract. Mech. , 803–837.
Tanguy, B., Luu, T., Perrin, G., Pineau, A., Besson, J., 2008. Plastic and damage behavior of a high strength X100 pipeline steel: experiments and modelling. Int. J. of Pressure Vessels and Piping 85, 322–335.
Tanné, E., Li, T., Bourdin, B., Marigo, J.J., Maurini, C., 2018. Crack nucleationfracture in variational phase-field models of brittle. J. Mech. Phys. Solids 110, 80–99.
Taylor, R., 2000. A mixed-enhanced formulation for tetrahedral finite elements. Int. J. Numer. Meth. Engng 47, 205–227.
Troiano, A., 2016. The role of hydrogen and other interstitials in the mechanical behavior of metals. Metallography, Microstructure, and Analysis 52, 147–157.
Tvergaard, V., 1982. Influence of void nucleation on ductile shear fracture at a free surface. J. Mech. Phys. Solids 30, 399–425.
Tvergaard, V., Needleman, A., 1995. Effects of nonlocal damage in porous plastic solids. Int. J. Solids Structures 32, 1063–1077.
Xia, Z., Zhang, J., Tong, Q., Ding, S., 2019. Multi-physics modeling of delayed hydride cracking in zirconium alloys. J. Mech. Phys. Solids 132.
Yu, H., Olsen, J., Alvaro, A., Qiao, L., He, J., Zhang, Z., 2019. Hydrogen informed Gurson model for hydrogen embrittlement simulation. Eng. Fract. Mech. 217.
Zhang, Y., Lorentz, E., Besson, J., 2018. Ductile damage modelling with locking-free regularised gtn model. Int. J. Numer. Meth. Engng 113, 1871–1903.
Zhang, Z., Thaulow, C., Ødegård, J., 2000. A complete Gurson model approach for ductile fracture. Eng. Fract. Mech. 67, 155–168.